
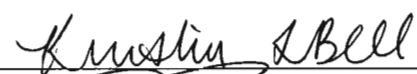
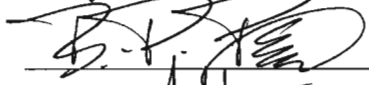




MEASUREMENT OF ANGULAR SPREAD OF SIGNALS IN SWELLEX-96 USING  
MULTITAPER ARRAY PROCESSING

by

Richard J. Wheelock  
A Thesis  
Submitted to the  
Graduate Faculty  
of  
George Mason University  
In Partial fulfillment of  
The Requirements for the Degree  
of  
Master of Science  
Electrical Engineering

Committee:

	Dr. Kathleen E. Wage, Thesis Director
	Dr. Kristine Bell, Committee Member
	Dr. Bernd-Peter Paris, Committee Member
	Dr. Andre Manitius, Chairman, Department of Electrical and Computer Engineering
	Dr. Lloyd J. Griffiths, Dean, The Volgenau School of Information Technology and Engineering

Date: August 1, 2008  
Summer Semester 2008  
George Mason University  
Fairfax, VA

Measurement of angular spread of signals in SWellEx-96 using multitaper array processing

A thesis submitted in partial fulfillment of the requirements for the degree of  
Master of Science at George Mason University

By

Richard J. Wheelock  
Bachelor of Science  
George Mason University, 2002

Director: Dr. Kathleen E. Wage, Professor  
Department of Electrical and Computer Engineering

Summer Semester 2008  
George Mason University  
Fairfax, VA

Copyright © 2008 by Richard J. Wheelock  
All Rights Reserved

## Dedication



## Acknowledgments

I gratefully acknowledge financial support from the following sources: Office of Naval Research Grant N00014-05-1-0639 and Navy STTR program Topic N04-T001: Shallow Water Beamformer.

# Table of Contents

	Page
List of Tables . . . . .	vii
List of Figures . . . . .	viii
Abstract . . . . .	xi
1 Introduction . . . . .	1
1.1 Array Processing . . . . .	1
1.2 The Shallow Water Environment . . . . .	1
1.3 Beamforming . . . . .	1
1.4 Multitaper Processing . . . . .	3
1.5 Spatial Spectrum . . . . .	4
1.6 The SWellEx-96 Dataset . . . . .	5
1.7 Goals . . . . .	5
1.8 Organization . . . . .	5
2 Background . . . . .	6
2.1 The SWellEx-96 Experiment . . . . .	6
2.1.1 The S5 Event . . . . .	6
2.1.2 The Horizontal Line Arrays . . . . .	7
2.1.3 Environment . . . . .	9
2.2 Summary . . . . .	12
3 Processing . . . . .	13
3.1 Preprocessing . . . . .	13
3.2 Beamformer Geometry . . . . .	14
3.3 Conventional Plane Wave Beamformer . . . . .	16
3.3.1 Array Sampling and Apertures . . . . .	19
3.3.2 Look Angle Sampling . . . . .	20
3.3.3 Beampatterns . . . . .	21
3.4 Conventional Spherical Wave Beamformer . . . . .	22
3.4.1 Beampatterns . . . . .	25
3.5 Minimum Power Distortionless Response Beamformer . . . . .	25

3.6	Summary . . . . .	31
4	Multitaper Processing . . . . .	32
4.1	Processor . . . . .	32
4.1.1	Beamspace Processor . . . . .	32
4.1.2	Planewave Detection . . . . .	34
4.2	Generalized Prolate Spheroidal Sequences . . . . .	35
4.2.1	The Constraints . . . . .	35
4.2.2	The Method . . . . .	36
4.2.3	The Tapers . . . . .	38
4.3	Summary . . . . .	38
5	Results . . . . .	44
5.1	Ray Simulations . . . . .	44
5.2	Number of Snapshots . . . . .	45
5.3	Horizontal Line Array North . . . . .	51
5.3.1	Close Range Source . . . . .	51
5.3.2	Long Range Source . . . . .	56
5.4	Horizontal Line Array South . . . . .	64
5.4.1	High Level Tones . . . . .	64
5.5	Summary . . . . .	71
6	Conclusion . . . . .	72
6.1	Concluding Comments . . . . .	72
6.2	Mismatch Issues . . . . .	73
6.3	Future Work . . . . .	73
	Bibliography . . . . .	75

## List of Tables

Table	Page
2.1 Shallow Source Tonal Set (C-109-9S) . . . . .	7
2.2 Deep Source Tonal Set (T-49-13) . . . . .	7



## List of Figures

Figure	Page
1.1 Example of multipath in a 213 meter wave guide. . . . .	2
1.2 Beamforming operation . . . . .	2
1.3 Spatial spectrum when a planewave is impinging on the array from 90 degrees	4
2.1 Average PSD . . . . .	8
2.2 S5 Event . . . . .	9
2.3 HLA North . . . . .	10
2.4 Deep Source Range to HLAN . . . . .	10
2.5 HLA North . . . . .	11
2.6 Deep Source Range to HLAS . . . . .	11
2.7 Sound Speed Profile . . . . .	12
3.1 Preprocessor . . . . .	14
3.2 Doppler Shift at 400Hz on HLA North and South . . . . .	15
3.3 The geometry of the beamformers . . . . .	16
3.4 The S5 tow track after transforming to array HLA North's beamforming axis. The original North, East coordinates are rotated 55 degrees clockwise . . .	17
3.5 The S5 tow track after transforming to array HLA South's beamforming axis. The original North, East coordinates are rotated 133 degrees clockwise . . .	17
3.6 Conventional planewave beampatterns at $\theta = 90$ degrees for 50Hz. Linear arrays have an ambiguity over 360 degrees that is broken when the array is non-linear . . . . .	20
3.7 The aesthetics of beamforming. Linear $u = \cos(\theta)$ spacing looks nicer. . . .	21
3.8 Beampatterns for the conventional planewave beamformer on HLA North .	23
3.9 Beampatterns for the conventional planewave beamformer on HLA South .	24
3.10 Spherical vs. Plane wave beampatterns at short range . . . . .	26
3.11 Spherical vs. Plane wave beampatterns at short range . . . . .	27
3.12 Geometry for Spherical Wave Beamformer in 2-dimensions. Extension to 3- dimensions is straight forward as it is only a range calculation. . . . .	28
3.13 Beampatterns for the conventional spherical wave beamformer on HLA North	29

3.14	Beampatterns for the conventional spherical wave beamformer on HLA South	30
4.1	Multitaper processor	33
4.2	The array sampling used for taper design. Only the x-coordinate is used from the element positions.	37
4.3	Eigenvalues and leakage for low, mid and high frequencies on HLA North. The dashed black lines show the array resolution ( $\lambda/aperture$ ) at each frequency.	39
4.4	Eigenvalues and leakage for low, mid and high frequencies on HLA South. The dashed black lines show the array resolution ( $\lambda/aperture$ ) at each frequency.	40
4.5	Analysis half-bandwidth for a frequency of 201Hz on HLA North. No plane wave is detected for an analysis band of $\pm 0.3$	41
4.6	HLA North tapers and their beampatterns for an analysis bandwidth of 0.1u. The dashed black lines show the analysis bandwidth.	42
4.7	HLA South tapers and their beampatterns for an analysis bandwidth of 0.1u. The dashed black lines show the analysis bandwidth.	43
5.1	Position of transmitter at 18 minutes, 30 seconds	46
5.2	Spatial spectra at close range (about 750 m) to HLA North for 201Hz using 1 snapshot of data.	47
5.3	Spatial spectra at close range (about 750 m) to HLA North for 201Hz using 4 snapshot of data.	48
5.4	Spatial spectra at close range (about 750 m) to HLA North for 201Hz using 10 snapshots of data.	49
5.5	Spatial spectra at close range (about 750 m) to HLA North for 201Hz using $2N = 54$ snapshots of data.	50
5.6	Position of transmitter at 22 minutes, 13 seconds	52
5.7	Ray paths from simulation at 750 meters	52
5.8	Spatial spectra at long range (about 4100 m) to HLA North for the 112Hz tone. 4 snapshots are used.	53
5.9	Spatial spectra at close range (about 750 m) to HLA North for 201Hz. 4 snapshots are used. The three arrivals estimated by ray simulations are easily seen in the output of the multitaper beamformer.	54

5.10	Raster plots of spatial spectra at close range (about 750 m) to HLA North for 201Hz on a dB scale. 4 snapshots are used at each time. The black marks indicate the arrivals from ray simulations . . . . .	55
5.11	Position of transmitter at 48 minutes, 7 seconds . . . . .	57
5.12	Ray paths from simulation at 4100 meters . . . . .	57
5.13	Spatial spectra at long range (about 4100 m) to HLA North for the high level tone 201Hz. 4 snapshots are used. The three arrivals estimated by ray simulations are easily seen in the output of the multitaper beamformer. . .	58
5.14	Spatial spectra at long range (about 4100 m) to HLA North for the high level tone 388Hz. 4 snapshots are used. No multipath is apparant on any beamformer at this frequency. . . . .	59
5.15	Spatial spectra at long range (about 4100 m) to HLA North for the high level tone 201Hz. $2N = 54$ snapshots are used. . . . .	60
5.16	Zoomed in on spatial spectra at long range (about 4100 m) to HLA North for the high level tone 201Hz. 4 snapshots are used. . . . .	61
5.17	Shallow source ray paths from simulation at 4100 meters . . . . .	62
5.18	Spatial spectra at long range (about 4100 m) to HLA North for the shallow source tone 198Hz. 4 snapshots are used. . . . .	63
5.19	Position of transmitter at 20 minutes, 6 seconds . . . . .	65
5.20	Ray paths from simulation at 2600 meters . . . . .	65
5.21	Spatial spectra at mid range (about 2600m) to HLA South for 201Hz. 4 snapshots are used. . . . .	66
5.22	Position of transmitter at 20 minutes, 6 seconds . . . . .	67
5.23	BTR at mid range (about 2600 m) to HLA South for 201Hz on a dB scale. 4 snapshots are used at each time. The black marks indicate the arrivals from ray simulations . . . . .	68
5.24	Spatial spectra at long range (about 2600 m) to HLA South for the low level tone 204Hz. 4 snapshots are used. . . . .	69
5.25	Spatial spectra at long range (about 2600 m) to HLA South for the low level tone 207Hz. 4 snapshots are used. . . . .	70

## **Abstract**

### MEASUREMENT OF ANGULAR SPREAD OF SIGNALS IN SWELLEX-96 USING MULTITAPER ARRAY PROCESSING

Richard J. Wheelock

George Mason University, 2008

Thesis Director: Dr. Kathleen E. Wage

Detection and bearing estimation in shallow water is difficult due to multipath. As array aperture increases, angular resolution increases and observation of multipath becomes more likely. The SWellEx-96 experiment provides a publicly available dataset along with detailed environmental information. Ray simulations suggest there are multiple arrival paths at the arrays of interest. This thesis explores whether the horizontal line arrays deployed in the SWellEx-96 experiment have enough angular resolution to observe multipath in their environment. In the context of bearing estimation, the traditional, well established techniques of conventional and minimum power distortionless response (MPDR) beamforming are compared to a new multitaper beamforming framework proposed by Wage. The SWellEx-96 dataset requires the design of tapers for irregularly sampled data as the arrays are non-uniformly spaced.

The multitaper array processor proves to be a useful tool, often displaying multipath arrivals more clearly than the conventional and MPDR beamformers.

# Chapter 1: Introduction

## 1.1 Array Processing

Array processing uses an array of sensors to extract information from spatially propagating signals. Having multiple sensors allows us to exploit spatial characteristics of a signal for any number of reasons. This thesis is concerned with using an array sensors for the purposes of estimating the angle of arrival of a signal, or bearing estimation of a source.

## 1.2 The Shallow Water Environment

Acoustic signals propagating in shallow water often travel on multiple paths connecting source and receiver. Figure 1.1 shows an example of this phenomenon known as *multipath*. The signal from each path impinges on the array at different angles of elevation leading to multiple bearing estimation angles from a single source, or *angular spread*

## 1.3 Beamforming

The concept of beamforming is to combine the signals from all the sensors of an array with a weighting such that signals arriving from a certain angle of interest, or look direction,  $\theta$ , are emphasized while signals from other directions are attenuated. Illustrated in Figure 1.2, the output of the beamformer for look direction  $\theta$  is

$$y_{\theta}(n) = \sum_{m=1}^M c_{\theta,m}^* x_m(n) = \mathbf{c}_{\theta}^H \mathbf{x}_n \quad (1.1)$$

where  $x_m(n)$  is the  $n$ th sample of the transmitted signal  $x(t)$  received at sensor  $m$ .  $M$  is

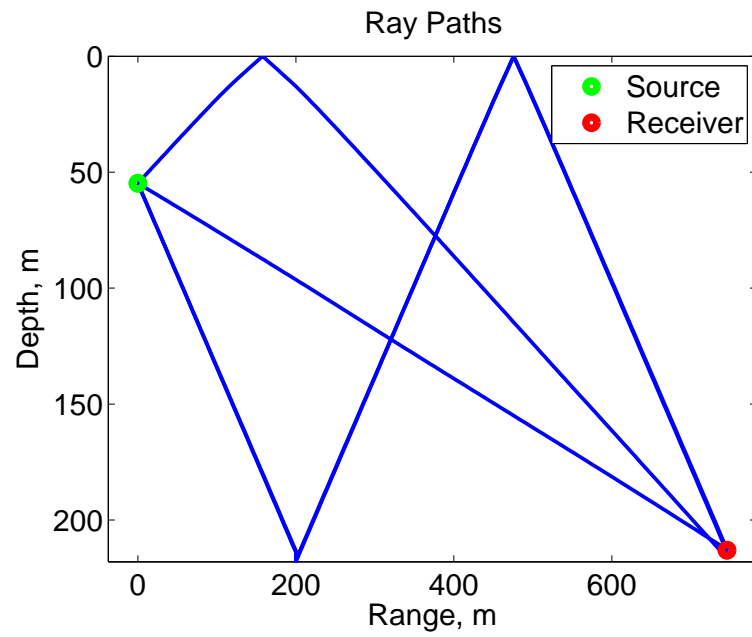


Figure 1.1: Example of multipath in a 213 meter wave guide.

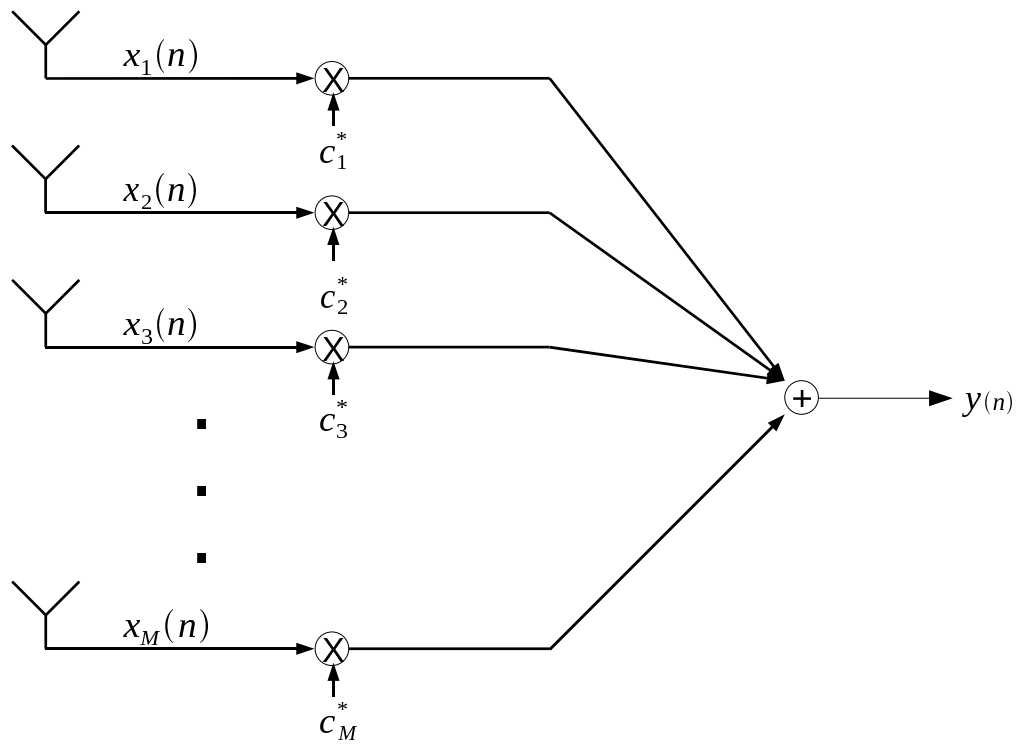


Figure 1.2: Beamforming operation

the number of sensors,  $y(n)$  is the output of the beamformer and

$$\mathbf{c}_\theta = \begin{bmatrix} c_{\theta,1} & c_{\theta,2} & c_{\theta,3} & \cdots & c_{\theta,M} \end{bmatrix}^T \quad (1.2)$$

$$\mathbf{x}_n = \begin{bmatrix} x_1(n) & x_2(n) & x_3(n) & \cdots & x_M(n) \end{bmatrix}^T \quad (1.3)$$

A number of resources provide detailed discussion of beamforming concepts and techniques for choosing the weight vector  $\mathbf{c}$  [1], [2], [3]. This thesis focuses on the ubiquitous conventional and minimum power distortionless response (MPDR) beamformers. The former is the spatial matched filter where  $\mathbf{c}$  is matched to a plane wave propagating from a direction of interest. The latter is a data-adaptive technique where  $\mathbf{c}$  is updated as new data arrives. This thesis also makes use of a new technique to bearing estimation, the *multitaper array processor*.

## 1.4 Multitaper Processing

The multitaper approach to spectral estimation was introduced by Thomson in 1982 as a way to reduce the variance and bias of single-snapshot power spectrum estimates [4]. Multiple orthogonal windows are used on a single snapshot of data as opposed to the Welch's method which uses averaging over multiple snapshots [9].

Wage has extended Thomson's method to spatial spectrum estimation by applying multiple tapers to a single spatial snapshot [5]. Application to the data set used in this thesis requires a set of orthogonal tapers for non-uniformly sampled data. Bronez proposed a procedure for the calculation of such tapers [6].

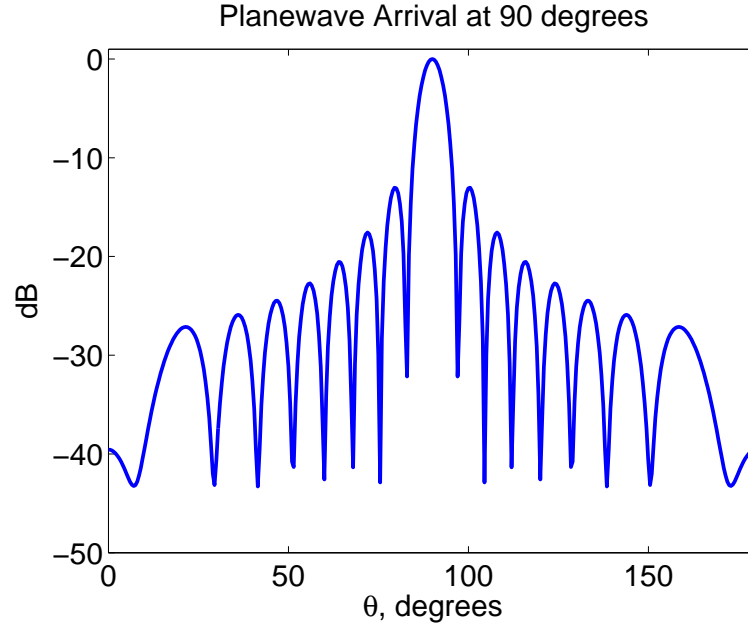


Figure 1.3: Spatial spectrum when a planewave is impinging on the array from 90 degrees

## 1.5 Spatial Spectrum

An array of sensors allows us to compute the *spatial spectrum* of spatially propagating signals impinging on the array. The spatial spectrum at angle  $\theta$  is  $E\{|y_\theta(n)|^2\}$  and is estimated by

$$S(\theta) = \frac{1}{N} \sum_{n=1}^N |y_\theta(n)|^2 \quad (1.4)$$

where  $N$  is the number of snapshots used in the average.  $\theta$  is varied over many angles. At directions from which signals are propagating, peaks occur in the spectrum giving us a bearing estimation of the source. For example, Figure 1.3 is the spatial spectrum when there is a single planewave source at 90 degrees to a particular array and a conventional beamformer is used and  $0 \leq \theta \leq 180$ .



## **1.6 The SWellEx-96 Dataset**

The SWellEx-96 experiment took place off the California coast in May 1996. In the experiment two acoustic sources were towed past a set of horizontal and vertical line arrays while transmitting narrowband tones. The data is publicly available.

## **1.7 Goals**

The main goal of this thesis is to evaluate the ability of the multitaper processor to observe angular spread in the SWellEx-96 data. The conventional and MPDR beamformers are used for comparison.

## **1.8 Organization**

This thesis is organized in the following way. Chapter 2 provides a detailed background to the SWellEx-96 experiment. Chapter 3 provides information on the pre-processing and implementation of the conventional and MPDR beamformers. A discussion of multitaper array processing follows in Chapter 4. The results of the beamforming techniques applied to the SWellEx-96 dataset are presented in Chapter 5.

## Chapter 2: Background

This chapter provides a detailed discription of the data set used in this thesis to compare beamforming techniques. The setup of the experiment is described including location and details of the acoustic source and arrays of interest. The basic outline of the acoustic propagation environment is then given.

### 2.1 The SWellEx-96 Experiment

The SWellEx-96 experiment took place off the California coast in May 1996. In this experiment, the R/V Sproul towed two acoustic sources transmitting narrowband tones past a set of vertical and horizontal receiving arrays. The SWellEx data set, which is publicly available via a website [7], consists of acoustic data for two events and a detailed set of environmental measurements. For this project, the data recorded on the two bottom-mounted horizontal line arrays (HLA's) is of particular interest because it offers an opportunity to investigate methods of bearing estimation.

#### 2.1.1 The S5 Event

The S5 event consists of two towed sources, one at 9 meters depth and the other at 54 meters depth. The shallow source transmitted the C-109-9S tonal set consisting of 9 tones between 109 Hz and 385 Hz shown in Table 2.1. The deep source transmitted the T-49-13 tonal set consisting of 65 tones between 49 Hz and 400 Hz at varying power levels. The tones are broken down into five sets of 13 tones with the first 13 being transmitted at a level of 158 dB and the next four sets transmitted at levels of 132, 128, 124 and 120 dB shown in Table 2.2. The power spectrum of the recorded data averaged over all hydrophones on

Table 2.1: Shallow Source Tonal Set (C-109-9S)

Frequency, Hz								
109	127	145	163	198	232	280	335	385

Table 2.2: Deep Source Tonal Set (T-49-13)

Level	Frequency, Hz												
158 dB	49	64	79	94	112	130	148	166	201	235	283	338	388
132 dB	52	67	82	97	115	133	151	169	204	238	286	341	391
128 dB	55	70	85	100	118	136	154	172	207	241	289	344	394
124 dB	58	73	88	103	121	139	157	175	210	244	292	347	397
120 dB	61	76	91	106	124	142	160	178	213	247	295	350	400

each HLA is shown in Figure 2.1. The high level deep source tones and the shallow source tones are aparent.

Shown in Figure 2.2, R/V Sproul started at a point southwest of HLA South and traveled in a northeasterly direction at about 5 knots passing HLA North. GPS data is provided for R/V Sproul throughout the event.

### 2.1.2 The Horizontal Line Arrays

#### Horizontal Line Array North

Horizontal Line Array (HLA) North is made up of 32 sensors spanning a 240 meter aperture lying at a depth of 213 meters. There were 5 bad sensors for a total of 27 processed hydrophones shown in Figure 2.3. The array is seen to be non-uniform and non-linear as there is a slight bow of about 15 meters. The line of bearing from the first element to the last is about 35 degrees clockwise from due north. Figure 2.4 shows the range from the deep source to the center of HLA North. The closest point of approach is about 700 meters and the furthest is about 4 kilometers.

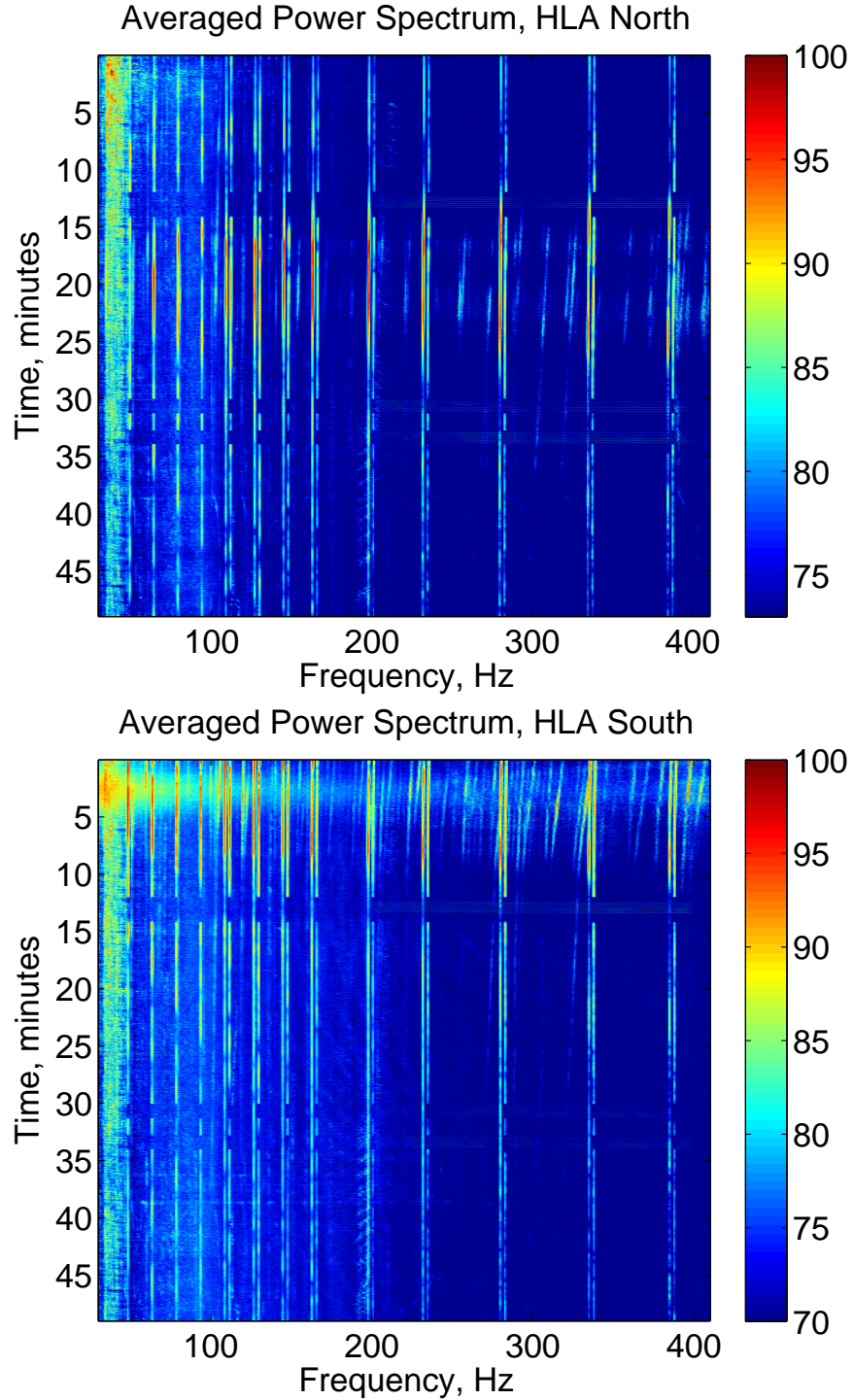


Figure 2.1: Averaged Power Spectrum over S5 event. At each hydrophone a 4192 point Hamming window is applied, an FFT is performed and then the magnitude is squared to get the power spectrum. The power spectrum from each sensor is then averaged together across each array. A 50% overlap is used between frames of data.

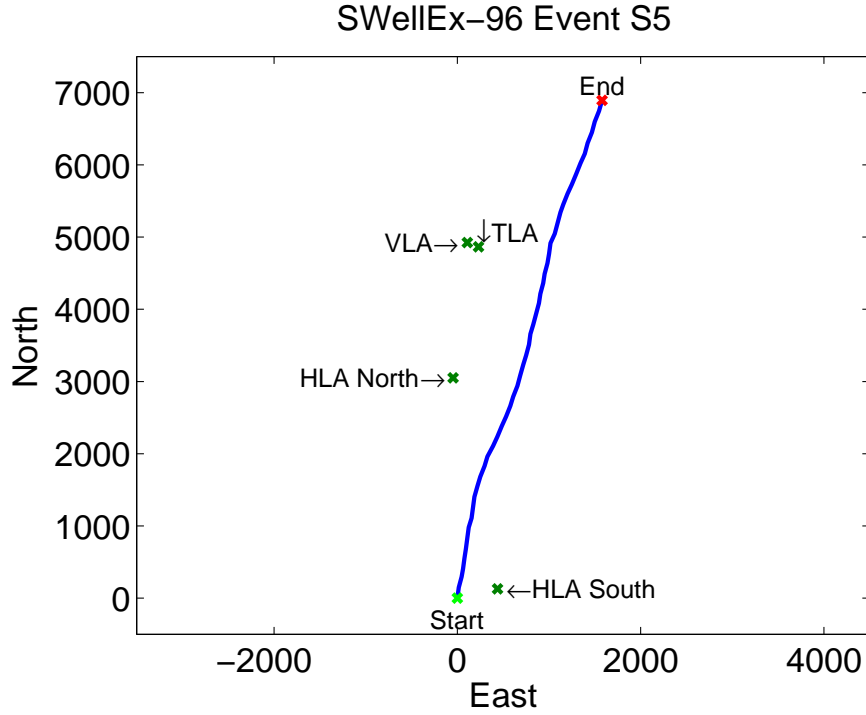


Figure 2.2: S5 Event Path of Sources

### Horizontal Line Array South

Horizontal Line Array South is again made up of 32 sensors but spans 255 meters and lies in slightly shallower water, at a depth of 198 meters. There were 4 bad sensors for a total of 28 hydrophones shown in Figure 2.5. Again the array is non-uniform and non-linear with a bow of about 10 meters. The line of bearing from the first element to the last is about 43 degrees counterclockwise from due north. Figure 2.6 shows the range from the deep source to the center of HLA South. The closest point of approach is about 350 meters and the furthest is almost 7 kilometers.

### 2.1.3 Environment

The area of the test site has been well studied providing detailed waveguide parameters. The sound speed profile of the water column is provided from conductivity, temperature and depth (CTD) measurements in the vicinity of the source tow. It is a downward refracting profile meaning propagation paths will tend to bend away from the surface towards the

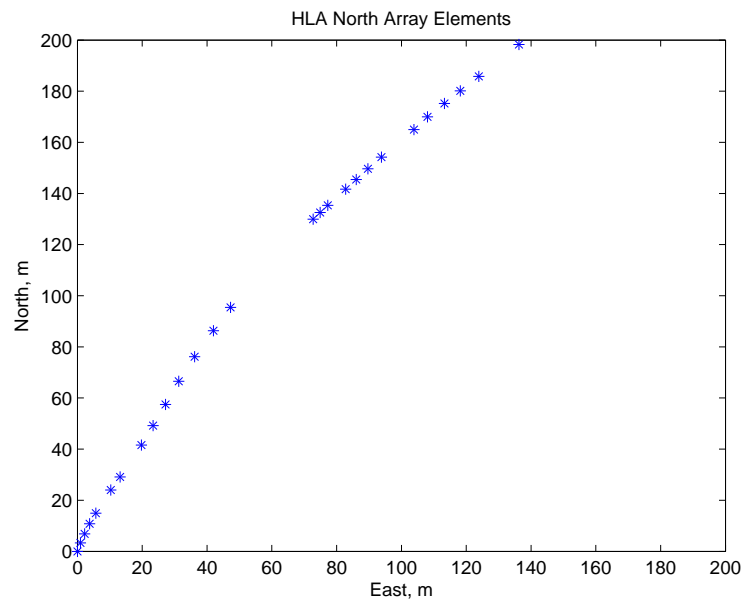


Figure 2.3: HLA North Sensor Positions

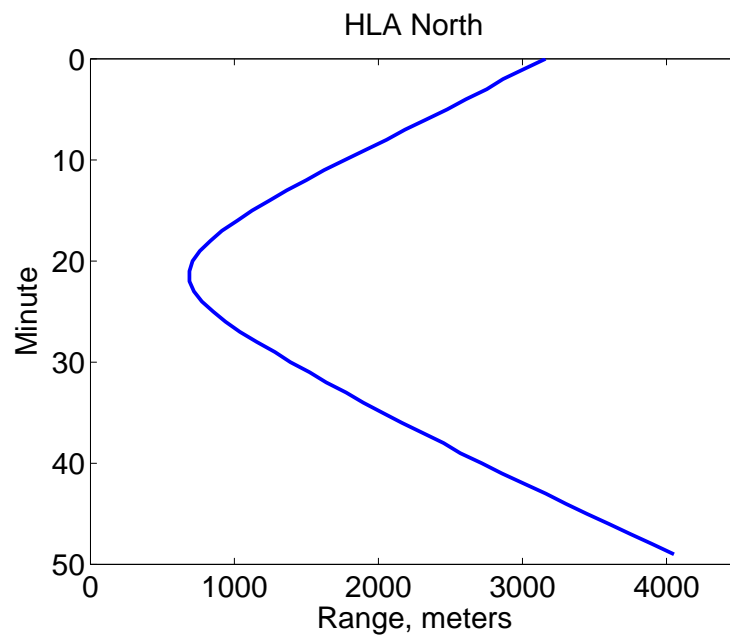


Figure 2.4: Range of Deep Source to Center of HLA North

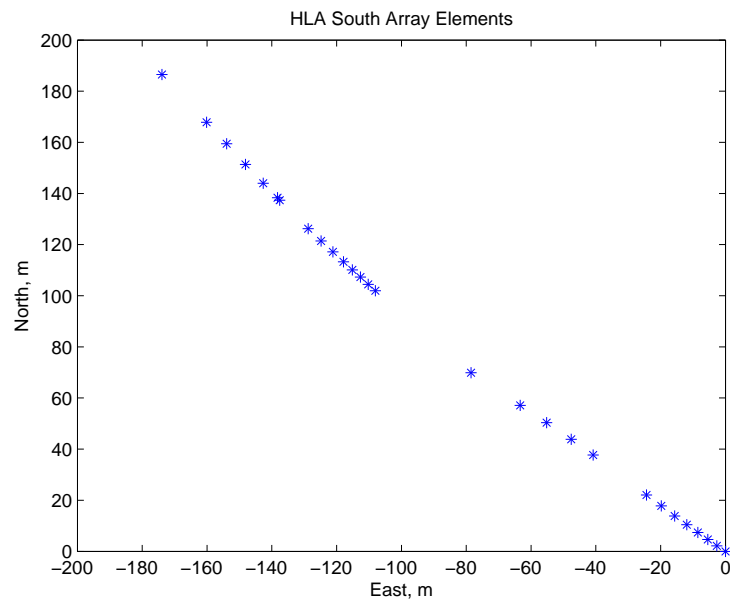


Figure 2.5: HLA South Sensor Positions

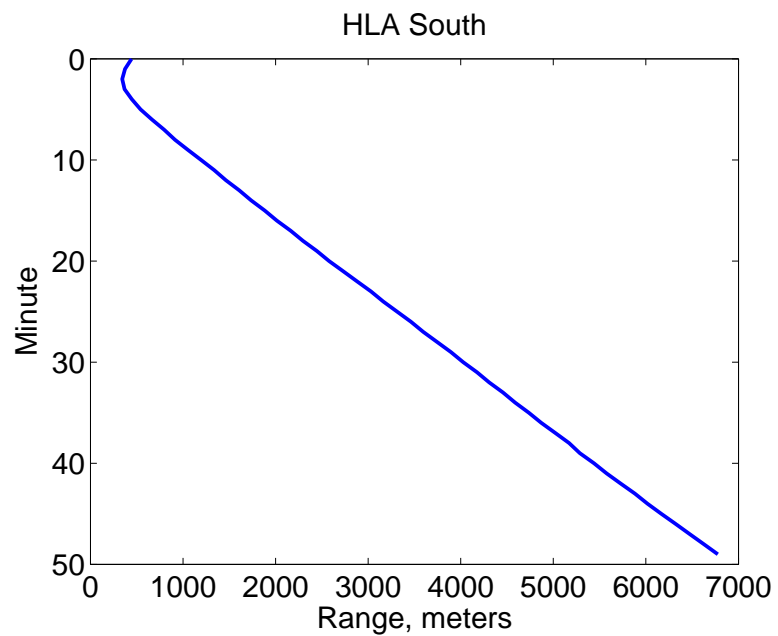


Figure 2.6: Range of Deep Source to Center of HLA South

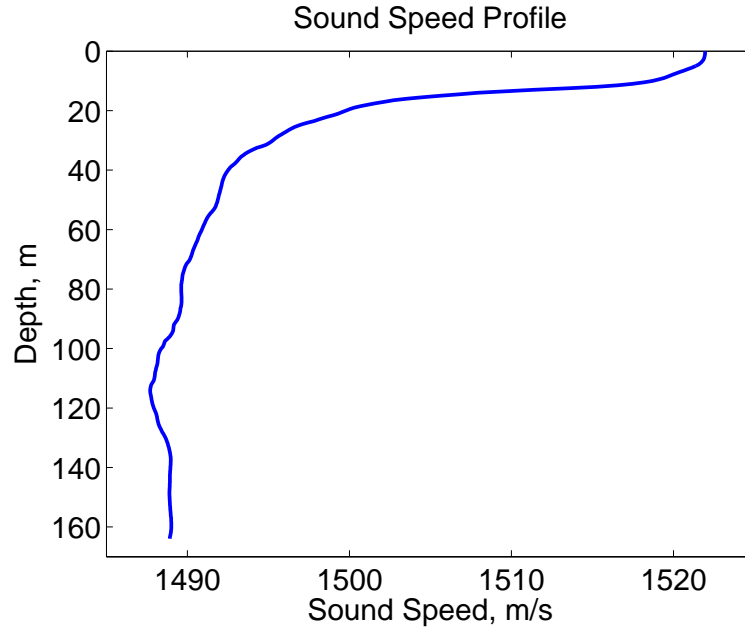


Figure 2.7: Sound Speed Profile

bottom where the sound speed is lower. Shown in Figure 2.7, it is used in simulations to predict arrival angles from a given position. The seafloor is made up of a 23.5 meters of sediment followed 800 meters of mudstone.

## 2.2 Summary

The SWellEx-96 experiment is over a decade old but is still one of the few publicly available underwater acoustic datasets. It provides the opportunity to work with real data in order to test the beamforming techniques presented in this thesis. Just as importantly, it provides positioning and environmental data to verify results.



## Chapter 3: Processing

In this thesis the spatial spectrum is of interest for purposes of bearing estimation. Obtaining the spatial spectrum requires a narrow band filter at the frequency of interest followed by beamforming at the angle of interest. This chapter starts by describing the pre-processor where the narrow band tuning is done. It then discusses the conventional beamformer in the context of plane and spherical wavefront beamforming. It then gives an outline of the MPDR beamformer.

### 3.1 Preprocessing

The pre-beamformer processing is the same for all beamformers examined. Shown in Figure 3.1, data is recorded at each sensor, it is windowed, then an FFT is performed and the frequency of interest is extracted from each sensor. This is equivalent to a narrowband filtering process. A Hamming taper is used in the windowing process to decrease the side-lobes of the FFT. The output of the preprocessor is  $\mathbf{p}(\Omega)$ , a column vector containing the frequency bin of interest from the FFT output at each sensor and  $\Omega$  is the frequency of interest.

Since the sources are moving, Doppler shift is a concern. Using the GPS positions of R/V Sproul the Doppler frequency,  $f'$ , is calculated with [8]

$$f' = \left( \frac{1}{1 + \frac{dr/dt}{c}} \right) f \quad (3.1)$$

where  $dr/dt$  is change in range with respect to time,  $c$  is the nominal sound speed which is assumed to be 1500 m/s and  $f$  is the frequency prior to Doppler effect. Figure 3.2 is a plot of

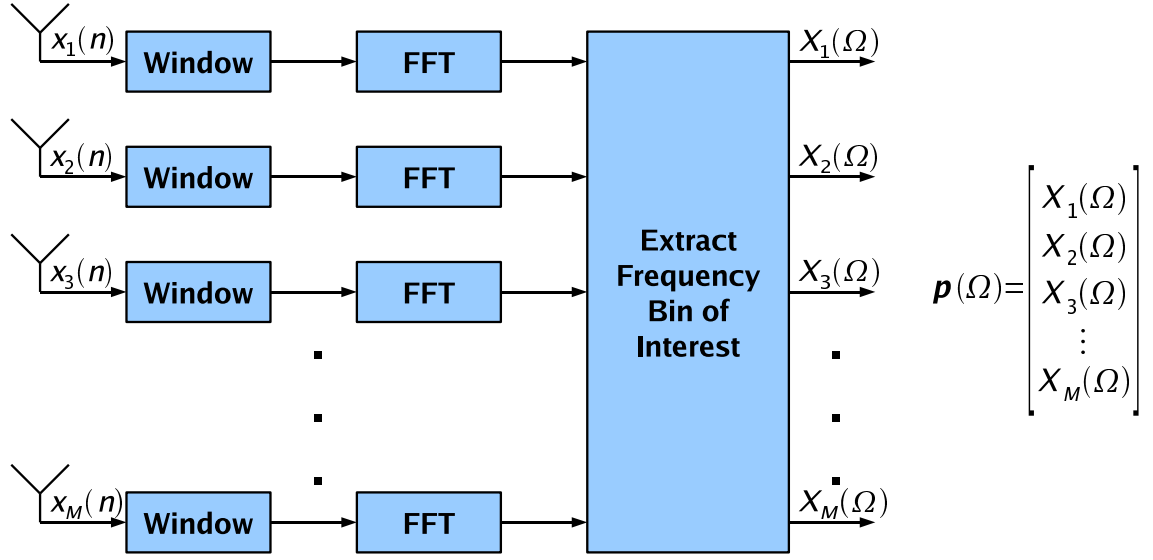


Figure 3.1: Preprocessor

$f' - f$ , the Doppler shift on HLA North and South where  $f = 400Hz$ , the highest frequency of the experiment suffering the most Doppler effect. The GPS data is only updated every 60 seconds so the plot is not smooth but a maximum shift of about  $\pm 0.7Hz$  is expected on both arrays.

The frequency shift can be accounted for in the preprocessor by taking a large enough FFT to bin the  $\pm 0.7Hz$  into a single frequency bin. The frequency spacing of the FFT is equal to  $\Delta f = \frac{f_s}{N_{FFT}}$ . With desired  $\Delta f \geq 1.4Hz$  and  $f_s = 3276.8Hz$ , the length of the FFT is  $N_{FFT} \leq 2341$ . Using the nearest power of 2 lower,  $N_{FFT} = 2048$  for all the processing presented in this document. An overlap factor of 50% is also used between temporal snapshots.

### 3.2 Beamformer Geometry

The coordinates of the arrays are given with respect to true north and east. As discussed in the previous chapter and seen in Figures 2.3 and 2.5, the line of bearing from the first point to the last does not lie on either the north or east axis. To help keep the output of the beamformers easier to understand, the beamforming (azimuthal) angle,  $\theta$ , is taken with

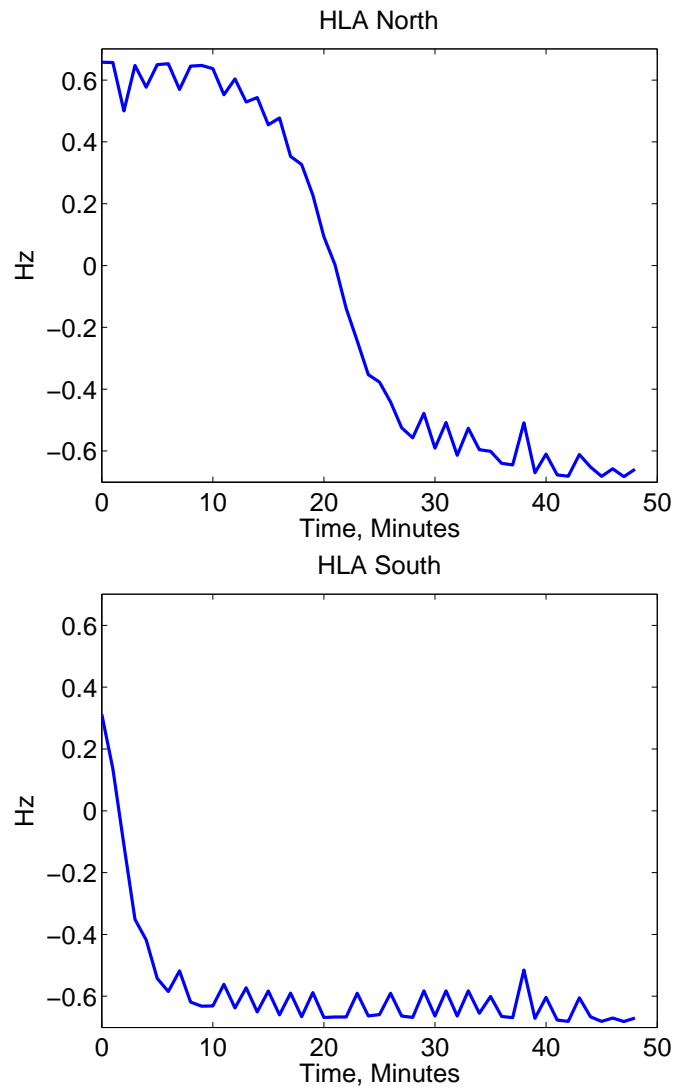


Figure 3.2: Doppler Shift at 400Hz on HLA North and South

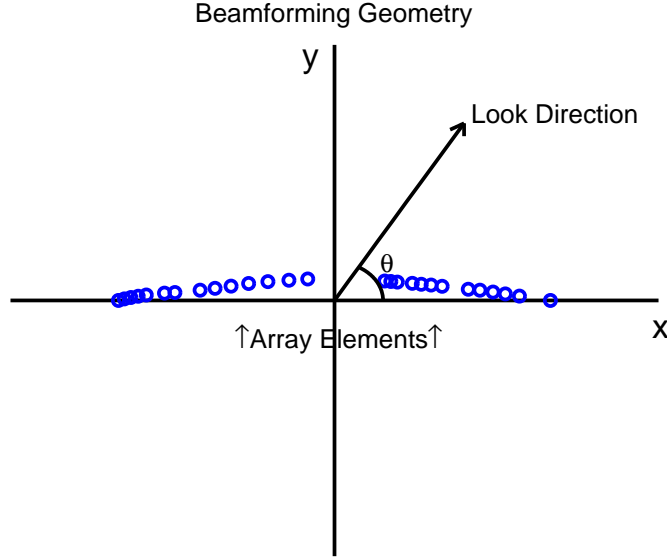


Figure 3.3: The geometry of the beamformers

respect to the axis,  $x$ , that connects the first and last element of the array and the axis,  $y$ , perpendicular to  $x$  and passing midway between the first and last element as shown in Figure 3.3.

The same rotation of positions are applied to the path of the source. Figures 3.4 and 3.5 show the arrays and source paths in the transformed coordinates for HLA North and South respectively.

### 3.3 Conventional Plane Wave Beamformer

A number of resources provide detailed discussions of beamforming in the context of array processing. The book by Van Trees [1] is a thorough reference on which the following discussion and notation is based.

A beamformer is a spatial filter that emphasizes a signal propagating from a 'look' direction while attenuating signals from other directions. That is, the phase at each of  $M$  array elements is matched to that of a signal propagating from a particular point or

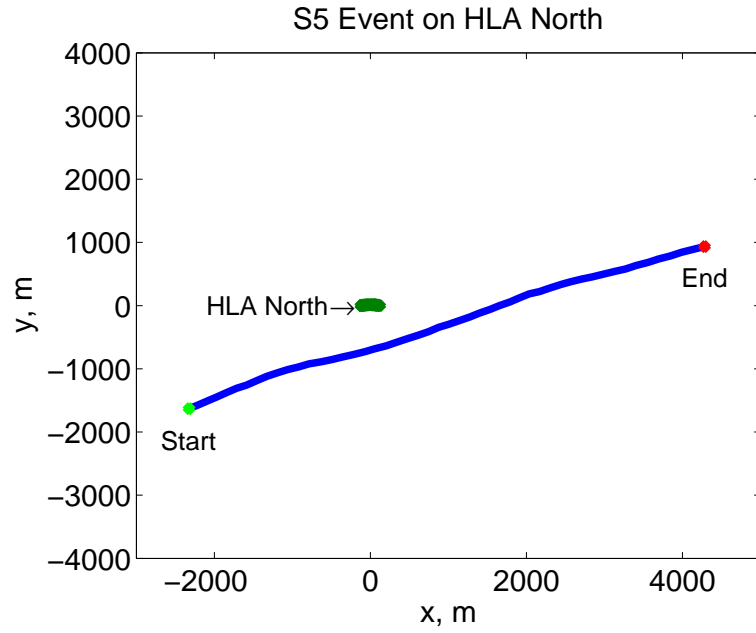


Figure 3.4: The S5 tow track after transforming to array HLA North's beamforming axis. The original North, East coordinates are rotated 55 degrees clockwise

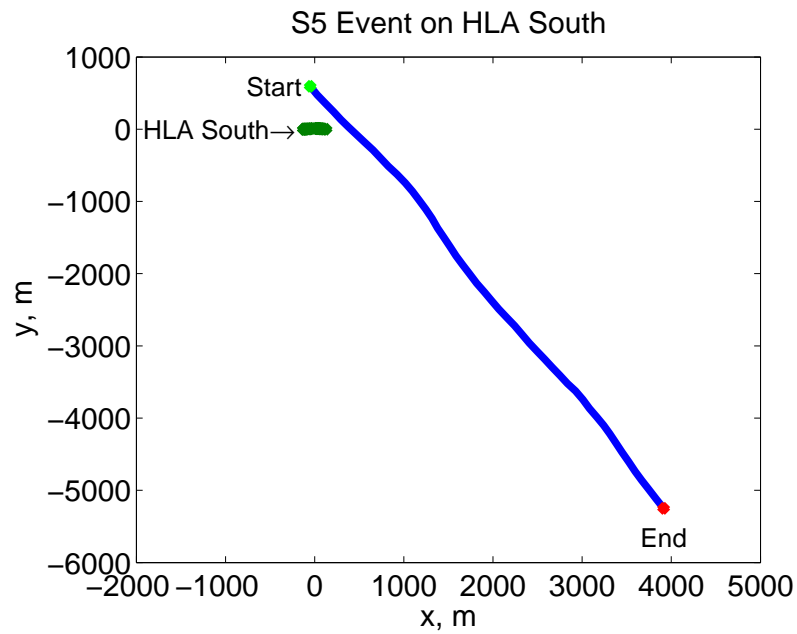


Figure 3.5: The S5 tow track after transforming to array HLA South's beamforming axis. The original North, East coordinates are rotated 133 degrees clockwise

direction. This information is captured in the array response vector  $\mathbf{v}$

$$\mathbf{v} = \begin{bmatrix} e^{-j\omega\tau_0} \\ e^{-j\omega\tau_1} \\ \vdots \\ e^{-j\omega\tau_{M-1}} \end{bmatrix} \quad (3.2)$$

where

$$\tau_m = \frac{r_m - r_o}{c} \quad (3.3)$$

where  $r_n$  is the range from source to the  $m$ th receiver,  $r_o$  is the range from source to the origin and  $c$  is the speed of propagation.

In the case of a plane wave propagating in 2-dimensions from distant a source

$$\omega\tau_m = \mathbf{k}^T \mathbf{p}_m \quad (3.4)$$

where  $\mathbf{k}$  is the wavenumber defined as

$$\mathbf{k} = -\frac{2\pi}{\lambda} \begin{bmatrix} \cos(\theta) \\ \sin(\theta) \end{bmatrix} \quad (3.5)$$

where  $\lambda$  is the wavelength of the signal of interest and  $\mathbf{p}_m$  is the position in  $x - y$  space of the  $m$ th array element

$$\mathbf{p}_m = \begin{bmatrix} x_m \\ y_m \end{bmatrix} \quad (3.6)$$

Then Equation 3.2 can be written as

$$\mathbf{v}_{\mathbf{k}} = \begin{bmatrix} e^{-j\mathbf{k}^T \mathbf{p}_0} \\ e^{-j\mathbf{k}^T \mathbf{p}_1} \\ \vdots \\ e^{-j\mathbf{k}^T \mathbf{p}_{M-1}} \end{bmatrix} = \mathbf{v}(\theta) \quad (3.7)$$

The parameter  $\theta$  is varied over the look directions of interest. The array response matrix is simply a collection of array response vectors at the look angles of interest,  $\theta_l$ ,  $l = 1, \dots, L$

$$\mathbf{W} = \begin{bmatrix} \mathbf{v}(\theta_1) & \mathbf{v}(\theta_2) & \dots & \mathbf{v}(\theta_L) \end{bmatrix} \quad (3.8)$$

The estimate of the spatial spectrum is the response to signals impinging on the array as the array response vector is steered over all angles averaged over  $N$  snapshots

$$\mathbf{S} = \frac{1}{N} \sum_{n=1}^N \mathbf{W}^H \mathbf{p}_n(\Omega) \quad (3.9)$$

A *beam pattern* is a useful tool for evaluating a beamformer. It gives us the angular response of a beamformer,  $\mathbf{c}$ , to a set of array response vectors over a number of angles

$$BP = |\mathbf{c}^H \mathbf{W}|^2 \quad (3.10)$$

### 3.3.1 Array Sampling and Apertures

Figure 3.6 presents some features of beam patterns for different arrays. For these plots  $\mathbf{c} = \mathbf{v}(90)$ , the beamformer is matched to a plane wave at broadside, and  $0 \leq \theta \leq 360$ . Figure 3.6(a) shows a beam pattern for a uniformly spaced linear array. The beam pattern is

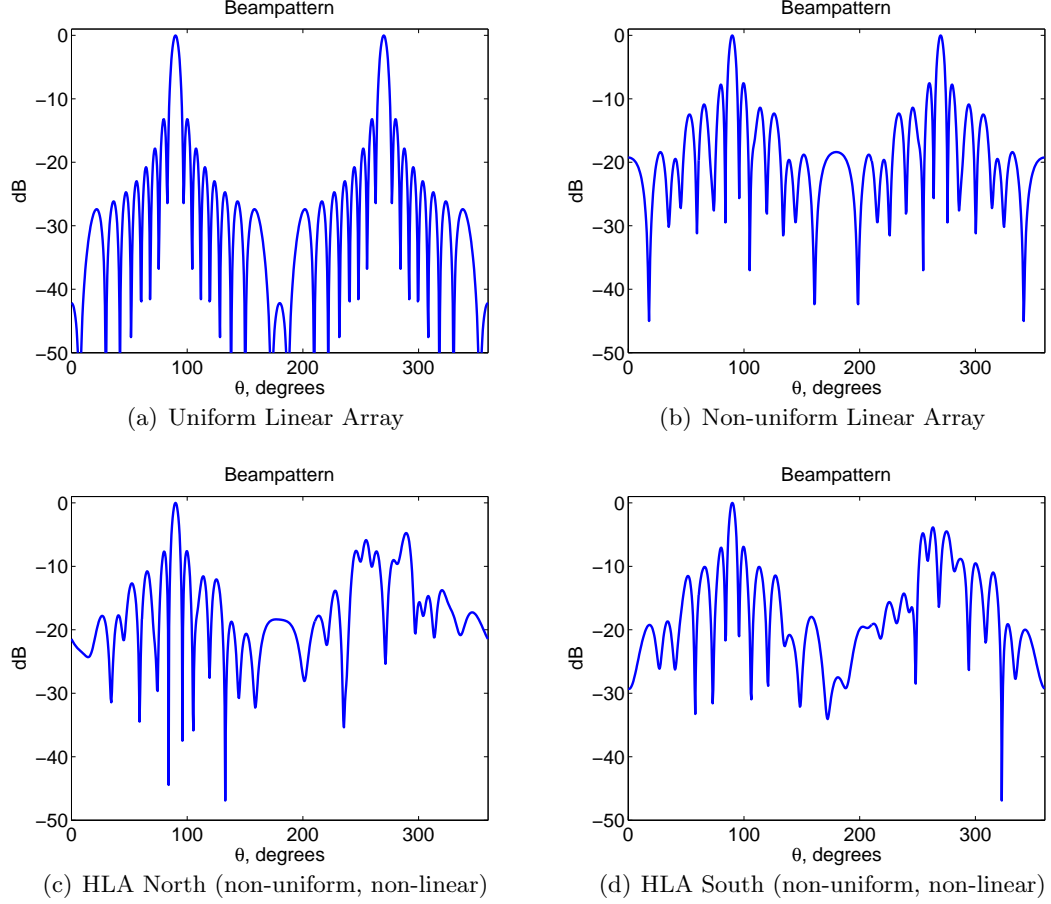


Figure 3.6: Conventional planewave beampatterns at  $\theta = 90$  degrees for 50Hz. Linear arrays have an ambiguity over 360 degrees that is broken when the array is non-linear

sinc like and repeats every 180 degrees. Figure 3.6(b) shows that a beampattern for a non-uniformly spaced linear array is less regular but still repeats every 180 degrees. This array is the x-coordinate of HLA North. Figures 3.6(c) and 3.6(d) show the beampatterns for the non-uniformly spaced, non-linear arrays, HLA North and South respectively. The periodicity of the linear aperture is broken by the bow in the arrays. The sidelobe performance is also worse in the case of irregular sampling compared to uniform sampling.

### 3.3.2 Look Angle Sampling

Throughout the rest of this thesis, beampatterns and spatial spectrum are shown for linear  $u = \cos(\theta)$  instead of linear  $\theta$  unless otherwise noted. The advantage of linear u-spacing



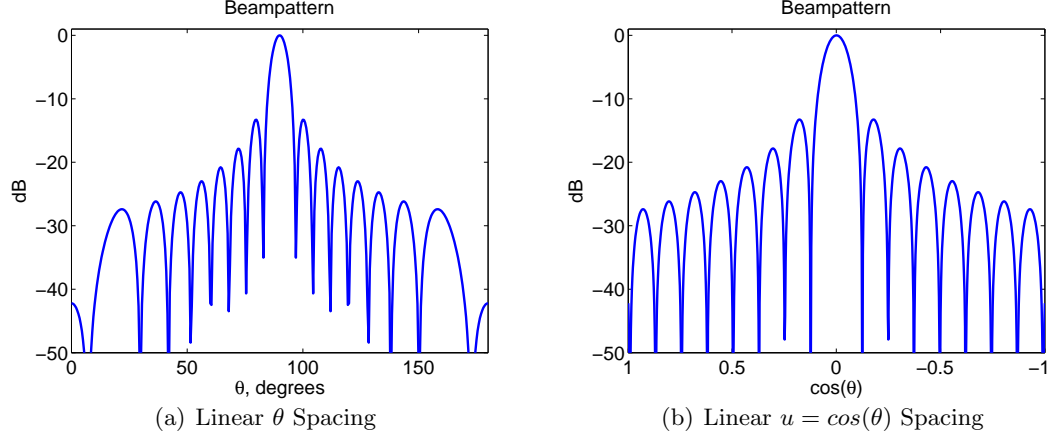


Figure 3.7: The aesthetics of beamforming. Linear  $u = \cos(\theta)$  spacing looks nicer.

is one of aesthetics. Figure 3.7 shows two beampatterns for the same beamformer. With linear  $\theta$  spacing in Figure 3.7(a), the beampattern is 'stretched out' towards endfire ( $\theta = 0$  or  $180$  degrees). With linear  $\cos(\theta)$  spacing in Figure 3.7(b) the beampattern looks more regularly spaced. Note that values of  $\cos(\theta)$  repeat on the intervals  $0 < \theta \leq 180$  and  $180 < \theta \leq 360$ . However, plots are generally only shown for  $1 \geq \cos(\theta) \geq -1$  ( $0 \leq \theta \leq 180$ ) or  $-1 \geq \cos(\theta) \geq 1$  ( $180 \leq \theta \leq 360$ ) so this ambiguity in  $u$  should not be an issue.

### 3.3.3 Beampatterns

Beampatterns for HLA North and South are shown in Figures 3.8 and 3.9 respectively for broadside ( $u = 0$  or  $\theta = 90$  degrees) and  $u = 0.9$  ( $\theta = 26$  degrees), near endfire ( $u = 1$  or  $\theta = 0$  degrees). The plots are shown for look angles  $0 \leq \theta \leq 180$  or  $1 \geq \cos(\theta) \geq -1$  and for frequencies of 50, 200 and 400 Hz, representative of the low, mid and high range of the SWellEx-96 transmitted frequencies.

It is apparant that as the frequency increases, the mainlobe of the beampattern becomes narrower. The half power point of the mainlobe in radians is approximated at broadside by [3]

$$\Delta_{3dB} \approx \frac{\lambda}{L} \quad (3.11)$$

where  $\lambda$  is the wavelength of the propagating signal and  $L$  is the aperture of the array in meters. As the frequency increases,  $\lambda$  decreases and we expect the mainlobe width to decrease.

### 3.4 Conventional Spherical Wave Beamformer

At times throughout event S5, the source is at a close enough range to each array that the standard planewave assumption is not valid. For example, Figures 3.10 and 3.11 shows the beampatterns at  $\cos(\theta) = 0$  ( $\theta = 90$  degrees) for plane and spherical wave beamformers at 200 Hz on a uniform linear array. The input array response vector is generated using the source range. Figure 3.10 shows the beampatterns for a source at 700 meters range (the closest point of approach to HLA North). In this case, the arrival is spread in angle around  $u = 0$  for the plane wave array response matrix,  $\mathbf{W}$ , but has a single peak when  $\mathbf{W}$  is generated for spherical wavefronts at that range. At this close range, the curvature of the wavefront must be taken into account when beamforming or the arrival will appear spread. Figure 3.11 shows the beampatterns when the impinging wavefront is generated from 7000m range (about the longest range from HLA South). In this long range case there is little difference between the spherical and plane wave beamformers. The curvature of the wavefront is negligible and can be approximated as a plane wave.

The method used to implement the spherical wavefront beamformer makes use of the GPS data from Event S5. From Equation 3.2, the quantities that are needed to calculate the array response vector,  $\mathbf{v}$ , are the time delay from source to receiver,  $\tau$ , and the radian frequency of the signal of interest,  $\omega$ . Using the GPS data, the range from the source to the center of the array is calculated at the time of interest. To build the  $\mathbf{W}$  matrix, a point is fixed at this range and elevation angle, then the azimuthal angle rotated around the center of the axis with an array response vector being calculated at each angle of interest. At each angle, the range and then, using  $c = 1500$  m/s, the time delay to each element,  $\tau_n$ , is calculated and the time to point (0,0) is subtracted out giving the differential delay to each element with respect to the origin. This is illustrated in Figure 3.12.  $\omega$  is fixed so  $\mathbf{v}$  is

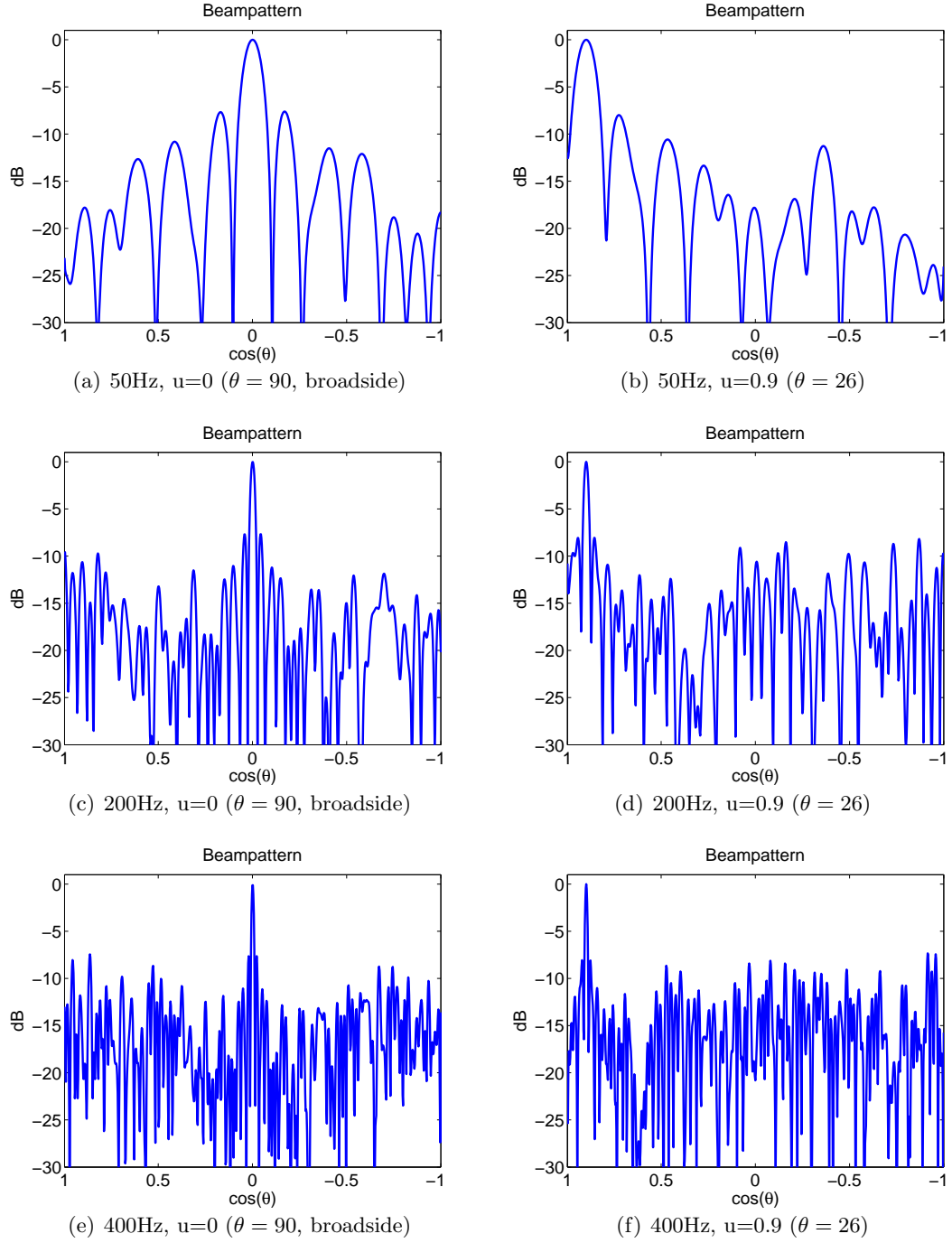


Figure 3.8: Beampatterns for the conventional planewave beamformer on HLA North

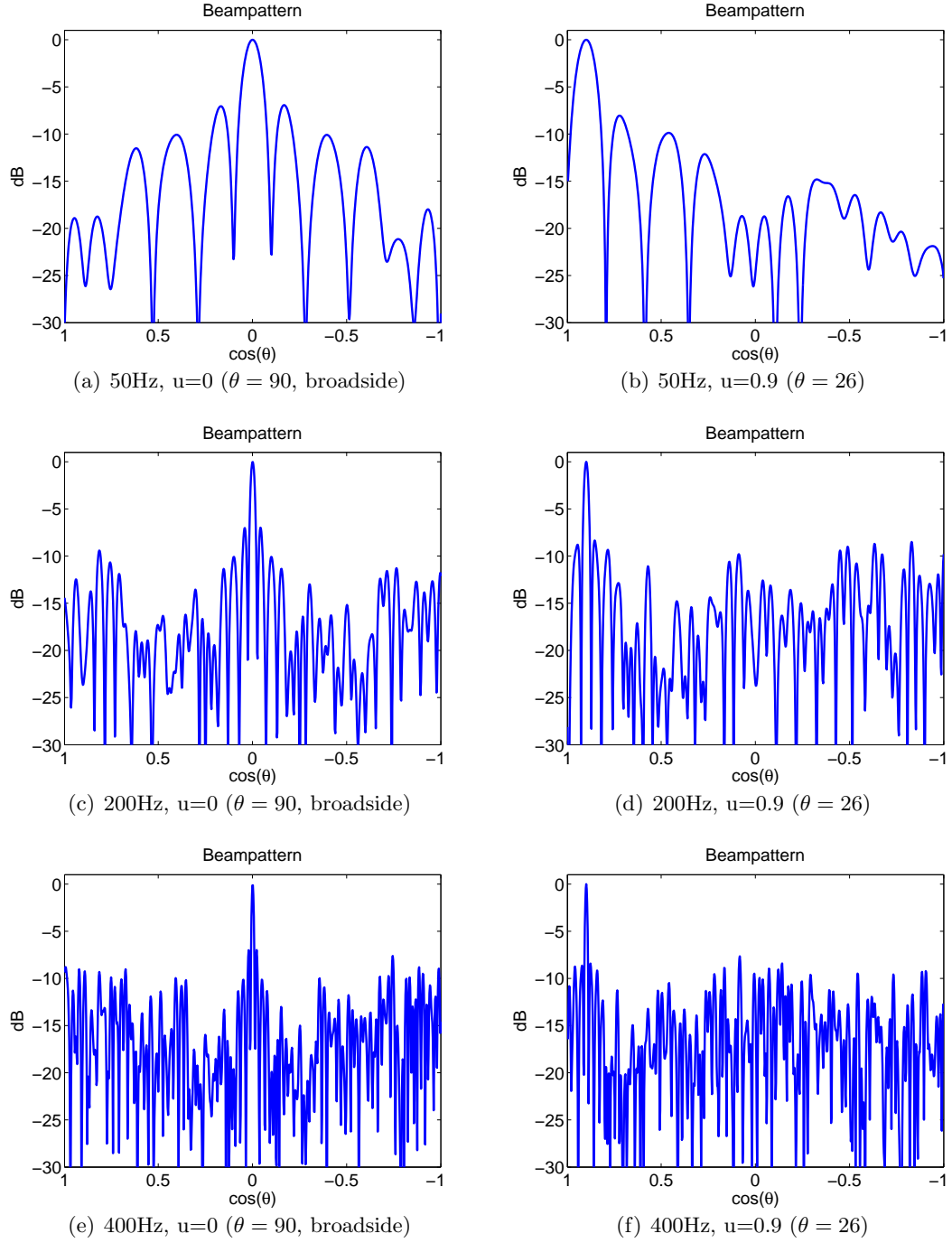


Figure 3.9: Beampatterns for the conventional planewave beamformer on HLA South

computed from Equations 3.2 and 3.3.

$$\mathbf{v} = \begin{bmatrix} e^{-j\omega\tau_0} \\ e^{-j\omega\tau_1} \\ \vdots \\ e^{-j\omega\tau_{M-1}} \end{bmatrix} = \begin{bmatrix} e^{-j\omega\frac{(r_0-r_o)}{c}} \\ e^{-j\omega\frac{(r_1-r_o)}{c}} \\ \vdots \\ e^{-j\omega\frac{(r_m-r_o)}{c}} \end{bmatrix} \quad (3.12)$$

### 3.4.1 Beampatterns

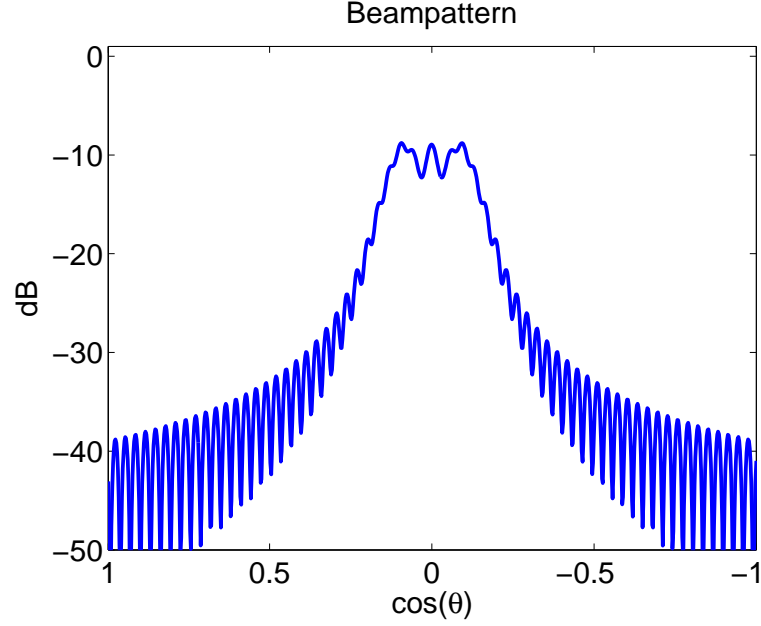
Figures 3.13 and 3.14 show the beampatterns for the HLA North and South respectively at angles of  $u = 0$  ( $\theta = 90$ ) and  $u = 0.9$  ( $\theta = 26$ ) for frequencies of 50, 200 and 400 Hz at a range of 700 *m* (the closest point of approach to HLA North.) The beampatterns are similar to those of the plane wave beamformer in Figures 3.8 and 3.9.

## 3.5 Minimum Power Distortionless Response Beamformer

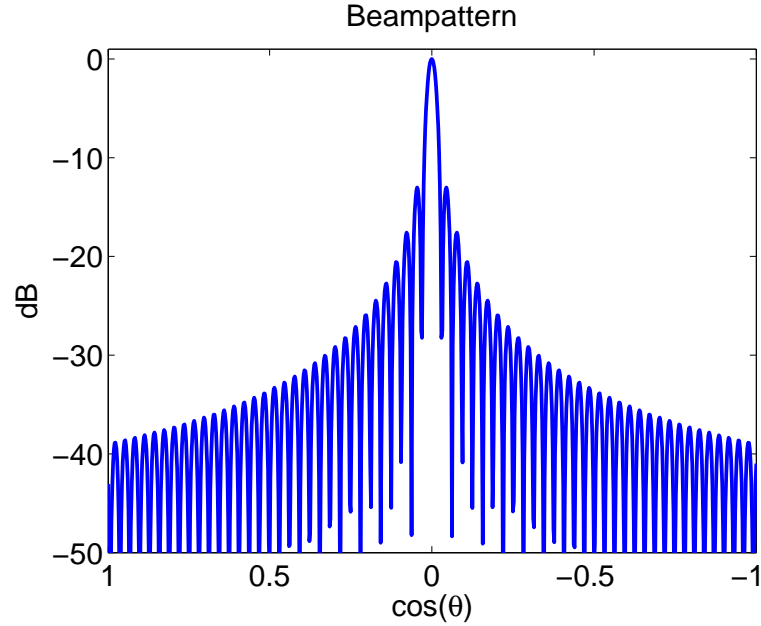
The minimum power distortionless response (MPDR) beamformer is a data-adaptive beamformer designed to minimize power from directions other than the look angle. That is, it will try to null out signals outside the look direction. If an array is receiving arrivals from multiple paths, the spatial spectrum of the MPDR beamformer can potentially show this clearer than that of the CBF, where the multipath may be obscured by the sidelobes.

Van Trees offers a full discussion and derivation for the MPDR beamformer [1]. The weight vector,  $\mathbf{c}$ , is matched to a wave front arriving from the look direction,  $\theta$ , while minimizing the total output power such that the power in the look direction is 1, or

$$\min \mathbf{c}^H \mathbf{R} \mathbf{c} \quad \text{s.t.} \quad \mathbf{c}^H \mathbf{v}(\theta) = 1 \quad (3.13)$$

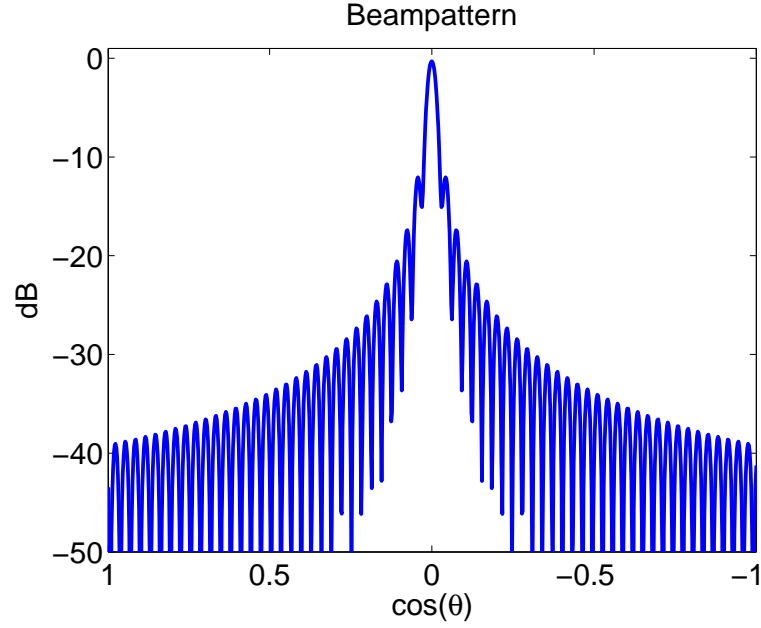


(a) Plane wave array response matrix,  $\mathbf{W}$

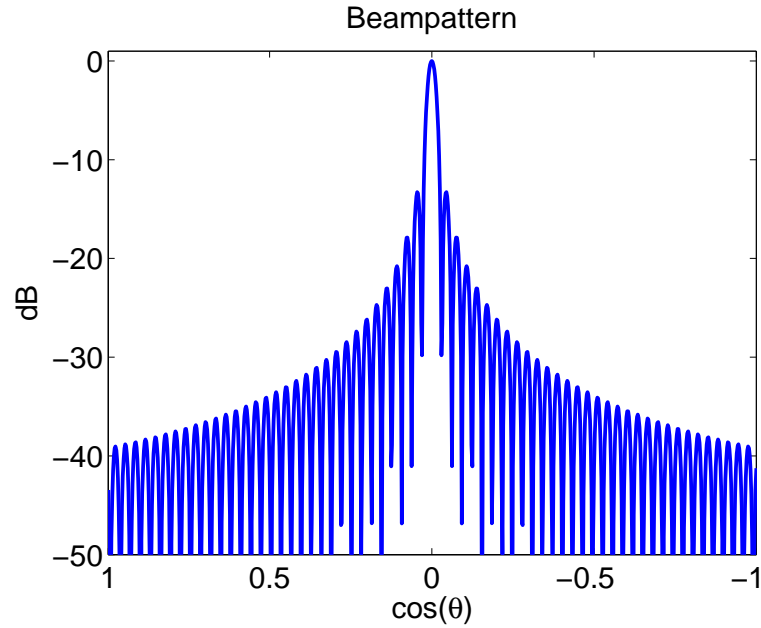


(b) Spherical wave array response matrix,  $\mathbf{W}$

Figure 3.10: Beampatterns at  $\cos(\theta) = 0$  (90 degrees) for the conventional plane and spherical wave beamformer on a uniform linear array at 700m range and frequency 200Hz. The wave front at  $\theta = 90$  degrees is generated using spherical waves. (a) is the beampattern when  $\mathbf{W}$  is generated for plane wavefronts. (b) is the beampattern when  $\mathbf{W}$  is generated for spherical wavefronts.



(a) Plane wave array response matrix,  $\mathbf{W}$



(b) Spherical wave array response matrix,  $\mathbf{W}$

Figure 3.11: Beampatterns at  $\cos(\theta) = 0$  (90 degrees) for the conventional plane and spherical wave beamformer on a uniform linear array at 7000m range and frequency 200Hz. The wave front at  $\theta = 90$  degrees is generated using spherical waves. (a) is the beampattern when  $\mathbf{W}$  is generated for plane wavefronts. (b) is the beampattern when  $\mathbf{W}$  is generated for spherical wavefronts.

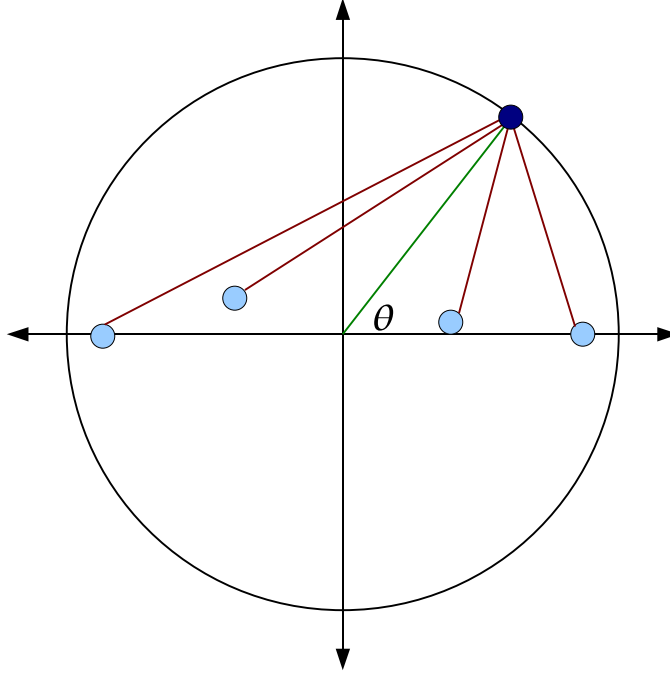


Figure 3.12: Geometry for Spherical Wave Beamformer in 2-dimensions. Extension to 3-dimensions is straight forward as it is only a range calculation.

where  $\mathbf{R}$  is the correlation matrix

$$\mathbf{R} = E\{\mathbf{p}(\Omega)\mathbf{p}^H(\Omega)\} \quad (3.14)$$

The distortionless filter,  $\mathbf{c}$ , is given by

$$\mathbf{c}_{MPDR}(\theta) = \frac{\mathbf{R}^{-1}\mathbf{v}(\theta)}{\mathbf{v}(\theta)^H \mathbf{R}^{-1}\mathbf{v}(\theta)} \quad (3.15)$$

One immediately apparent problem with Equation 3.15 is that  $\mathbf{R}$ , the received sample covariance, must be computed from *a priori* knowledge or estimated from data

$$\hat{\mathbf{R}} = \frac{1}{K} \sum_{k=1}^K \mathbf{p}_k \mathbf{p}_k^H + \gamma \mathbf{I} \quad (3.16)$$

where  $\mathbf{p}_k$  is the  $k$ th data snapshot from the preprocessor and  $\gamma$  is an optional *diagonal*



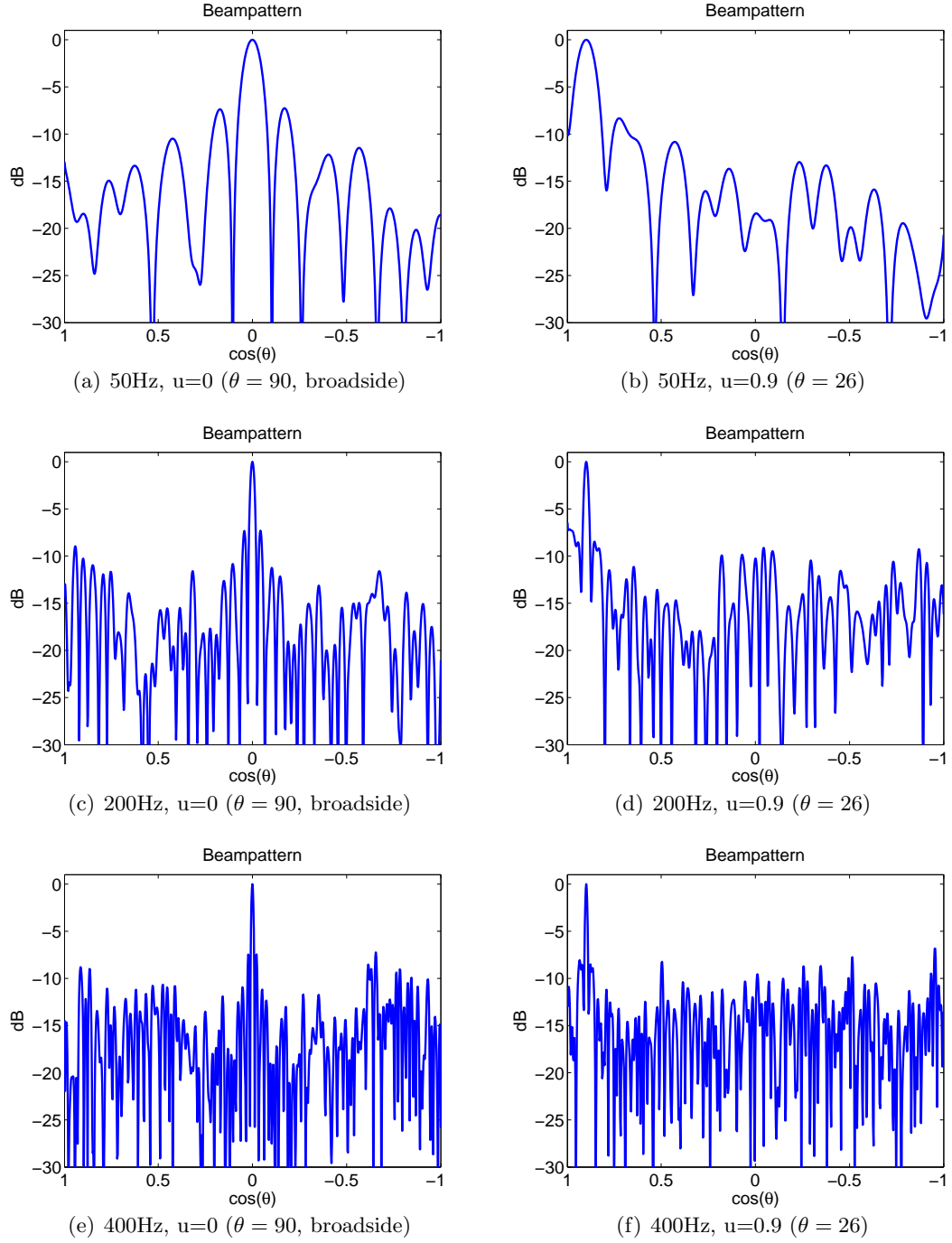


Figure 3.13: Beampatterns for the conventional spherical wave beamformer on HLA North

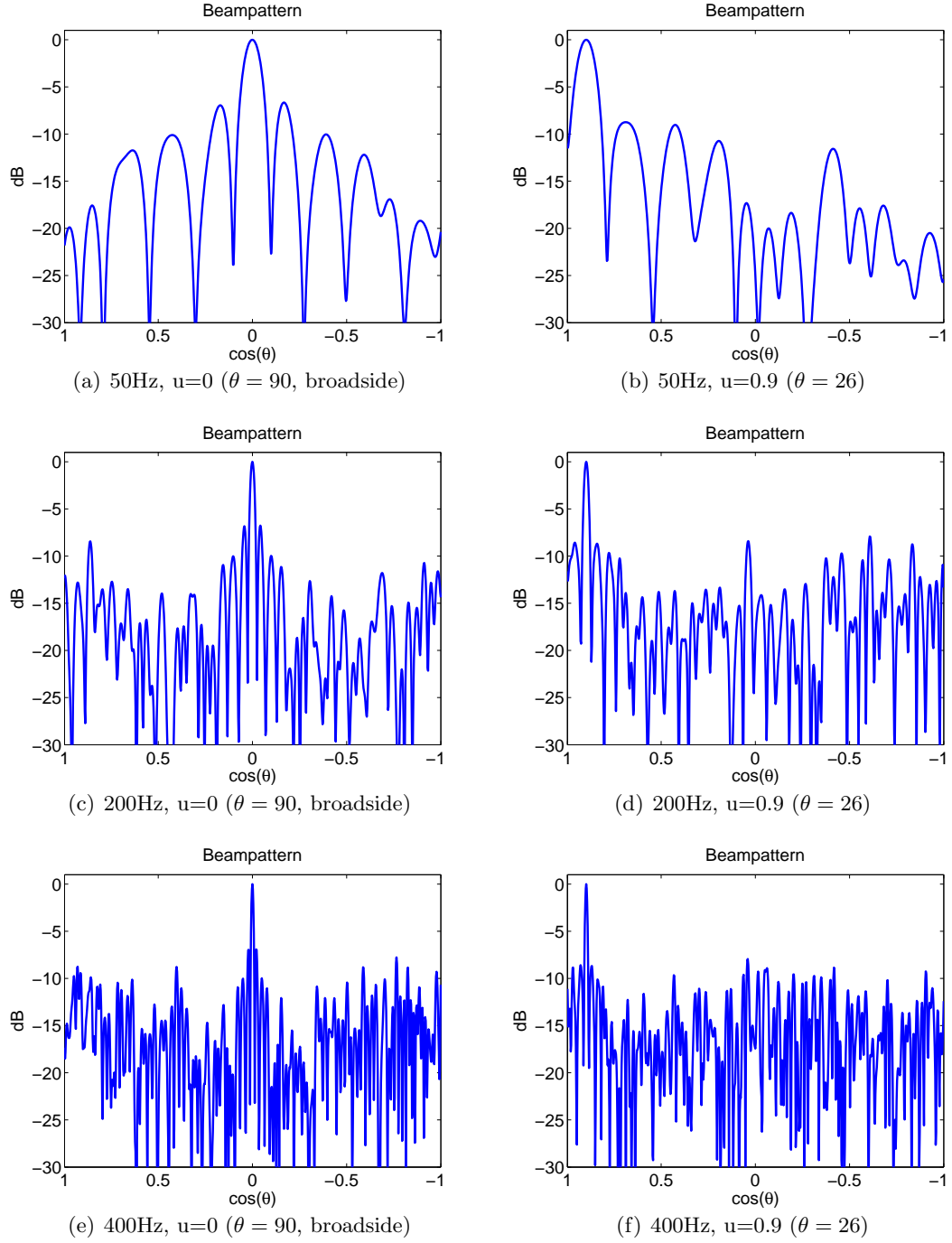


Figure 3.14: Beampatterns for the conventional spherical wave beamformer on HLA South

*loading* factor. Diagonal loading can help stabilize the inverse of  $\hat{\mathbf{R}}$ , particularly in the case of limited snapshots when  $K < N$  [1]. The processing here uses a diagonal loading factor of  $\gamma = 0.1tr\{\hat{\mathbf{R}}\}$ . Diagonal loading decreases the interference nulling effects of the MPDR beamformer, however.

### 3.6 Summary

This chapter provided an outline of the geometry, pre-processing and the traditional array processing methods of conventional and MPDR beamforming. The issue of Doppler shift is accounted for in the preprocessor. The issue of wave front curvature at close range is factored the into array response vectors.

## Chapter 4: Multitaper Processing

Thomson proposed the multitaper method as a way to decrease the variance of a spectral estimate with low sample support [4]. The commonly used method introduced by Welch improves variance by averaging over a number of snapshots [9]. The multitaper approach typically operates on a single data snapshot, applying multiple, orthonormal tapers (windows) and averaging the spectra obtained from each window to drive down variance.

The multitaper method has found use in time series analysis. The first part of this chapter describes the multitaper spatial spectrum estimation framework proposed by Wage [5]. It is followed by a discussion of computing orthonormal tapers for the case of irregularly sampled data by the method proposed by Bronez [6] [11].

### 4.1 Processor

The preprocessor from section 3.1 is used as the input to the multitaper array processor shown in Figure 4.1. The discussion in this section is based on the paper by Wage [5].

#### 4.1.1 Beamspace Processor

The multitaper array processor is a *beamspace* processor. The input data,  $\mathbf{p}(\Omega)$ , is projected onto a set of orthogonal beams centered around the angle of interest,  $\theta$ .

$$\mathbf{q}(\theta, \Omega) = \mathbf{W}_{MT}^H(\theta) \mathbf{p}(\Omega) \quad (4.1)$$

where the beamspace is contained in the columns of matrix  $\mathbf{W}_{MT}(\theta)$ . The  $k$ th column of  $\mathbf{W}_{MT}(\theta)$  is the array response vector  $\mathbf{v}(\theta)$  multiplied by taper  $\mathbf{u}_k$

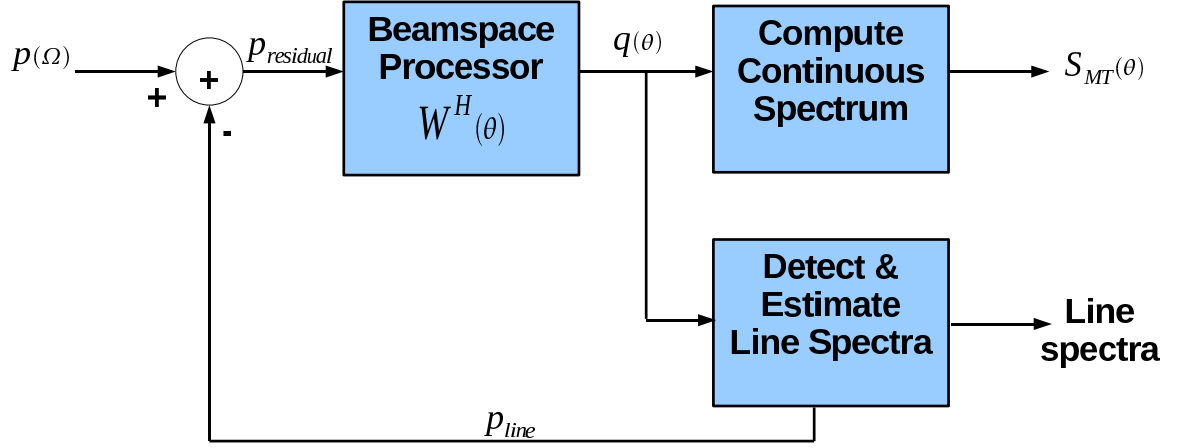


Figure 4.1: Multitaper processor

$$\mathbf{w}_k(\theta) = \mathbf{u}_k \odot \mathbf{v}(\theta) \quad (4.2)$$

each  $\mathbf{w}_k(\theta)$  is orthogonal. Putting them together in the columns of the matrix  $\mathbf{W}_{MT}(\theta)$

$$\mathbf{W}_{MT}(\theta) = \begin{bmatrix} \mathbf{w}_1 & \mathbf{w}_2 & \cdots & \mathbf{w}_K \end{bmatrix} \quad (4.3)$$

the columns are now an orthogonal beamspace.

The output of the beamspace processor,  $\mathbf{q}$ , is a K-dimensional vector. The output is averaged together to obtain the multitaper spatial spectrum estimate at angle  $\theta$

$$S_{MT}(\theta) = \sum_{k=1}^K \alpha_k |q_k(\theta)|^2 \quad (4.4)$$

Thomson outlines an adaptive method for calculating the weights  $\alpha_k$  that is used by the multitaper processor [4]. Basically, the tapers with larger amounts of energy outside of the region of interest are given less weighting in the estimate.

### 4.1.2 Planewave Detection

The continuous spatial spectrum is estimated by Equation 4.4 but the line components must be estimated separately. The multitaper processor uses a constant false alarm rate (CFAR) detector proposed by Jin and Friedlander to detect planewave arrivals [10].

A planewave arrival plus noise is modeled as

$$\mathbf{p} = \tilde{b}\mathbf{v}(\theta) + \mathbf{n} \quad (4.5)$$

The output of the  $k$ th taper steered towards  $\theta$  is

$$q_k(\theta) = \mathbf{w}_k^H(\theta)\mathbf{p} = \tilde{b}\mu_k + \mathbf{w}_k^H(\theta)\mathbf{n} \quad (4.6)$$

where  $\mu_k$  is the DC component of the  $k$ th taper

$$\mu_k = \sum_{n=1}^N u_k(n) \quad (4.7)$$

The output of the beamspace processor is then

$$q_k(\theta) = \mathbf{W}_{beam}^H(\theta)\mathbf{p} = \tilde{b}\boldsymbol{\mu} + \text{noise} \quad (4.8)$$

Linear regression gives an estimate of the complex amplitude  $\tilde{b}$

$$\hat{b}(\theta) = (\boldsymbol{\mu}^H \boldsymbol{\mu})^{-1} \boldsymbol{\mu}^H \mathbf{q}(\theta) \quad (4.9)$$

A CFAR statistic for detecting the presence of a single planewave in noise is

$$\frac{\mathbf{q}^H \mathbf{P}_\mu \mathbf{q}}{\mathbf{q}^H \mathbf{P}_{orth} \mathbf{q}} \sim F \text{ statistic}, \quad (4.10)$$

where  $P_\mu$  is the projection matrix for the subspace spanned by the vector  $\mu$  and  $P_{orth} = I - P_\mu$ , the projection into the orthogonal subspace. The test statistic can be averaged over L snapshots

$$\frac{\sum_l \mathbf{q}_l^H P_\mu \mathbf{q}_l}{\sum_l \mathbf{q}_l^H P_{orth} \mathbf{q}_l} \quad (4.11)$$

The probability of false alarm used throughout this thesis is 0.001.

## 4.2 Generalized Prolate Spheroidal Sequences

Discrete prolate spheroidal sequences (DPSS) are Thomson's tapers of choice because they are designed to maximize the power concentrated in a narrow angular region. DPSS tapers are designed for uniformly sampled data. However, SWellEx-96 array data is not uniformly sampled. Bronez proposes a method for the calculation of generalized prolate spheroidal sequences (GPSS) as tapers for irregularly sampled data [6] [11]. This section summarizes Bronez's method for computation of GPSS.

### 4.2.1 The Constraints

The multitaper method is trying to estimate the integrated spectrum:

$$P_A = \frac{1}{2\pi} \int_A S(\theta) d\theta \quad (4.12)$$

The analysis band A determines the resolution  $A_{min} \leq k_x \leq A_{max}$  The Bronez optimization criteria is

- Guarantee unbiased estimate when  $S(\theta)$  is flat across the signal band
- Minimize variance
- Minimize mount of bias due to signals outside of analysis band, or "global bias"

### 4.2.2 The Method

In the uniform sampling case, the DPSS are the solutions to an eigenvalue problem. In the non-uniform sampling case, the GPSS are the solution to the generalized eigenvalue problem:

$$\mathbf{R}_A \mathbf{w}_k = \lambda_k \mathbf{R}_B \mathbf{w}_k, \quad 1 \leq k \leq N \quad (4.13)$$

where  $\lambda_k \geq \lambda_{k+1}$  and the matrices  $\mathbf{R}_B$  and  $\mathbf{R}_A$  are given by

$$\mathbf{R}_B(n, m) = \int_B e^{j2\pi f(x_n - x_m)} df, \quad 1 \leq n \leq N, \quad 1 \leq m \leq N \quad (4.14)$$

$$\mathbf{R}_A(n, m) = \int_A e^{j2\pi f(x_n - x_m)} df, \quad 1 \leq n \leq N, \quad 1 \leq m \leq N \quad (4.15)$$

$B$  is the the *resolution bandwidth*. The *visible region* defined by Van Trees as  $\pm 2\pi/\lambda$ , where  $\lambda$  is the wavelength of the signal of interest is used as the resolution bandwidth [1]. The eigenvectors are normalized such that

$$\mathbf{w}_k^* \mathbf{R}_\alpha \mathbf{w}_k = \frac{|\alpha|}{K}, \quad 1 \leq k \leq K \quad (4.16)$$

The variance factor for  $K$  tapers is bound by

$$V\{\mathbf{w}_1, \dots, \mathbf{w}_k\} = \frac{|A|^2}{K} \quad (4.17)$$

and the bias factor is bound by

$$B\{\mathbf{w}_1, \dots, \mathbf{w}_k\} = \frac{|A|}{K} \sum_{k=1}^K (1 - \lambda_k) \quad (4.18)$$



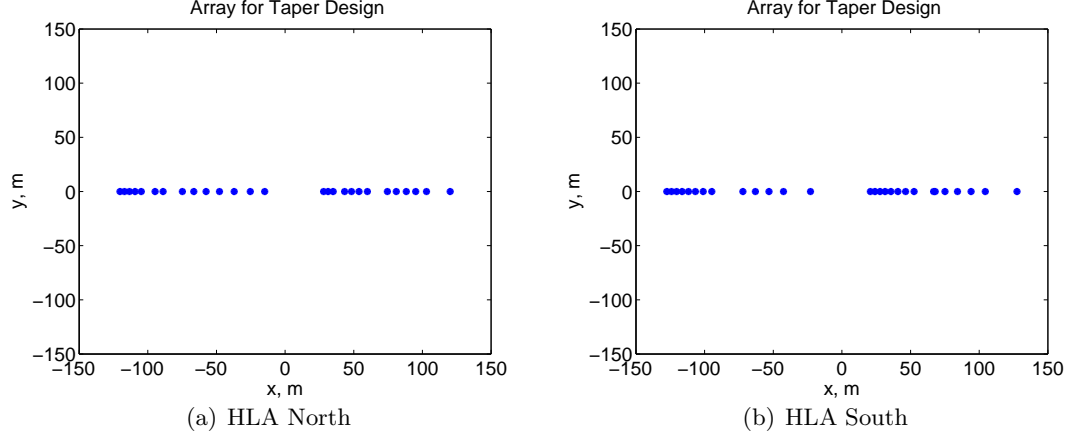


Figure 4.2: The array sampling used for taper design. Only the x-coordinate is used from the element positions.

so as the number of tapers,  $K$ , is increased, variance is decreased but the bias is increased.

Leakage for the  $k$ th taper  $\mathbf{w}_k$  is defined as

$$\gamma_k = 10 \log_{10}(1 - \lambda_k) \quad (4.19)$$

and represents the portion of energy falling outside the analysis band  $\alpha$  in decibels.

For the SWellEx-96 case, the y-coordinate of the array is ignored in the taper design. Figure 4.2 shows the array setup used for calculation of GPSS

Figure 4.3 shows the eigenvalues and leakage for tapers designed for HLA North at 50, 200 and 400Hz Bronez discusses that eigenvalues near 1 are desirable as they have less leakage. Using 6 tapers on the North array, the minimum analysis bandwidth would be upwards of about  $A = \pm 0.3u$  in order to get eigenvalues close to 1. However, the CFAR detector used in the multitaper processor can only handle 1 planewave in the analysis band and a width of  $0.3u$  is too wide for the angular spread seen on this array. Figure 4.5 shows the output of the multitaper processor at 201 Hz when the source is about 4100 meters range from HLA North. There should be at least one arrival around the magenta dots on the plots. In the case of a  $\pm 0.1u$  analysis bandwidth, there are two arrivals visible. For the analysis bandwidth of  $\pm 0.3u$ , there are no arrivals visible. This particular cut of data was

one of a number that seemed to yield better results with the smaller analysis bandwidth and is explored further in the following chapter. When set to a higher width, the multipath arrivals are often within the analysis bandwidth and so the detector breaks down.

Unless otherwise noted, 6 taper designed for an analysis half-bandwidth of  $0.1u$  centered around  $\theta = 0$  are used.

Figure 4.3 suggests that the North and South arrays are not designed well for higher frequencies around 400Hz. In fact HLA North has no elements within half a wavelength of each other and HLA South has only 1 pair. For this reason processing the lower frequencies is the focus.

The current implementation of the multitaper processor is thought to be sub-optimal for the non-uniform array case. Bronez's method suggests that tapers should be calculated for each angle of interest. However, the current processor calculates only the taper centered around  $\theta = 0$  and applies it to the array response vectors at all angles. This is standard practice in the case of uniformly sampled arrays where the output of a beamformer is equivalent to a downconversion to baseband, or  $\theta = 0$ , and the taper is at baseband. It is unclear at this time if that is the optimal thing to do in the irregularly sampled data case.

### 4.2.3 The Tapers

The tapers their beampatterns for HLA North and South for an analysis band width of  $\alpha = \pm 0.1u$  for frequency 201Hz are shown in Figures 4.6 and 4.7. The resolution bandwidth is  $\beta = \pm 1u$ . Though they are irregular in shape, their beampatterns have significant energy in the analysis band. The sidelobes are high as is expected from the leakage plots. For tapers 3-6 on both arrays, the leakage is particularly high near endfire.

## 4.3 Summary

This section presented the framework of Wage's multitaper array processor. One aspect of the multitaper process that had to be addressed was taper design for irregularly sampled data as the SWellEx-96 arrays are not uniformly spaced. Bronez provided the method for

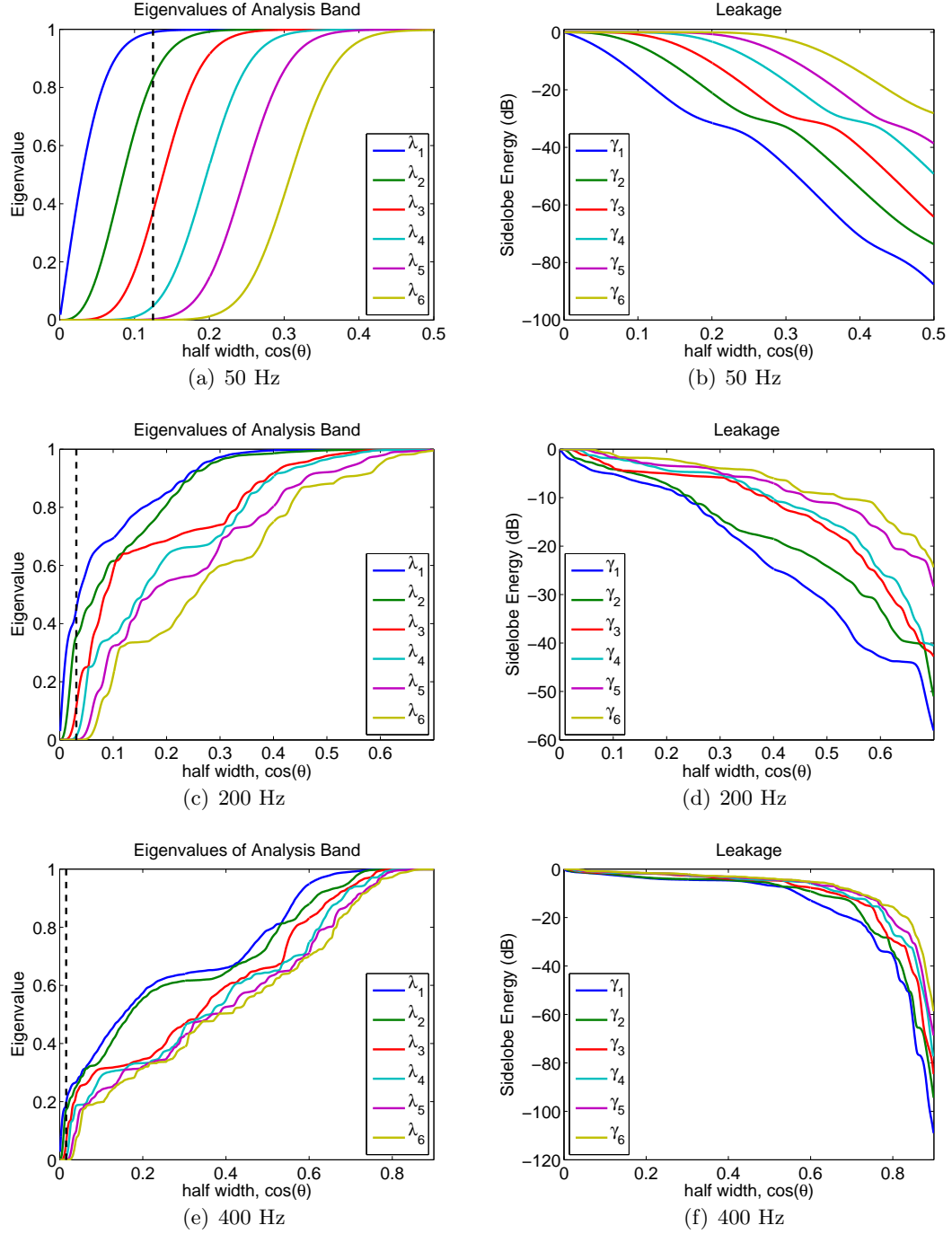


Figure 4.3: Eigenvalues and leakage for low, mid and high frequencies on HLA North. The dashed black lines show the array resolution ( $\lambda/\text{aperture}$ ) at each frequency.

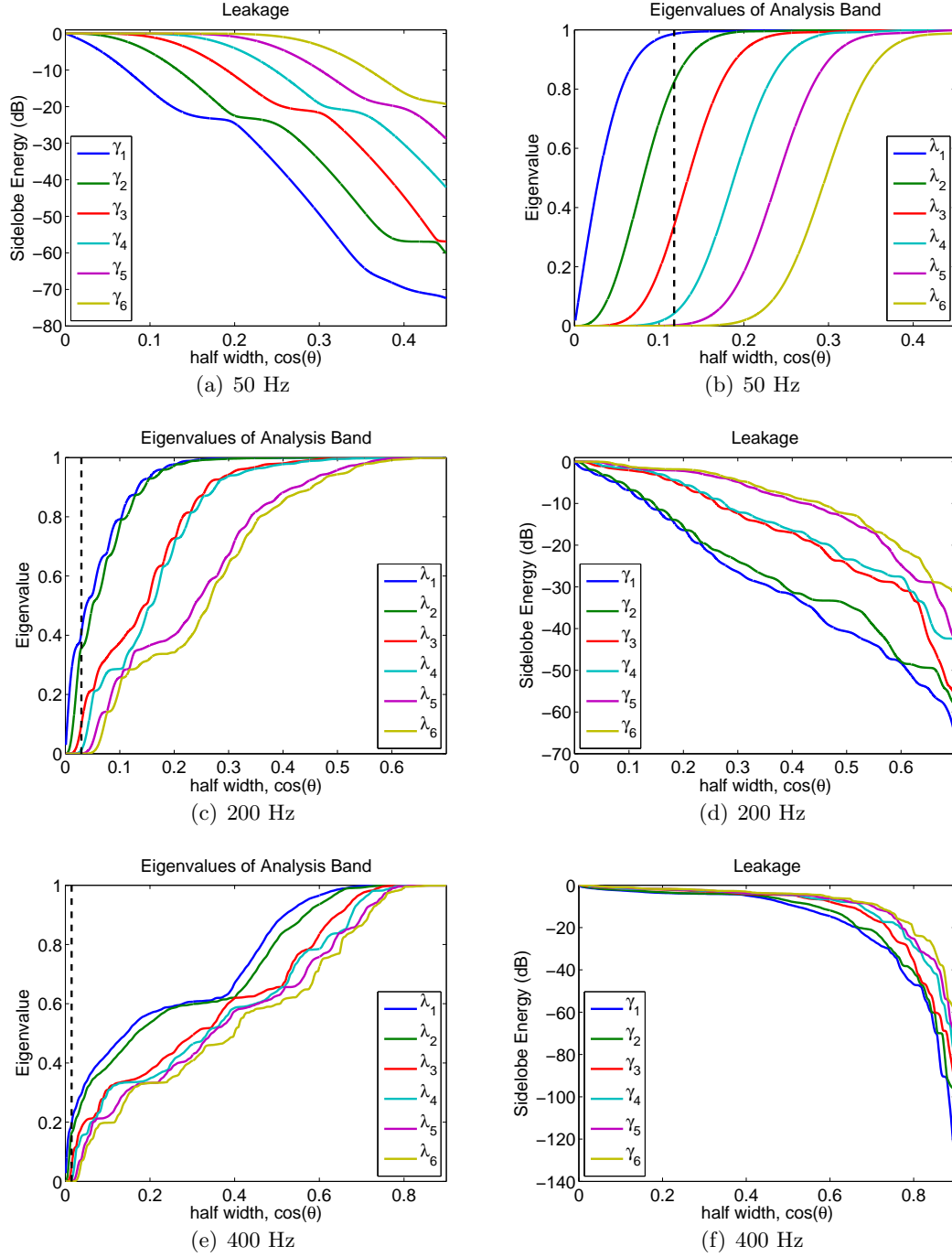


Figure 4.4: Eigenvalues and leakage for low, mid and high frequencies on HLA South. The dashed black lines show the array resolution ( $\lambda/aperture$ ) at each frequency.

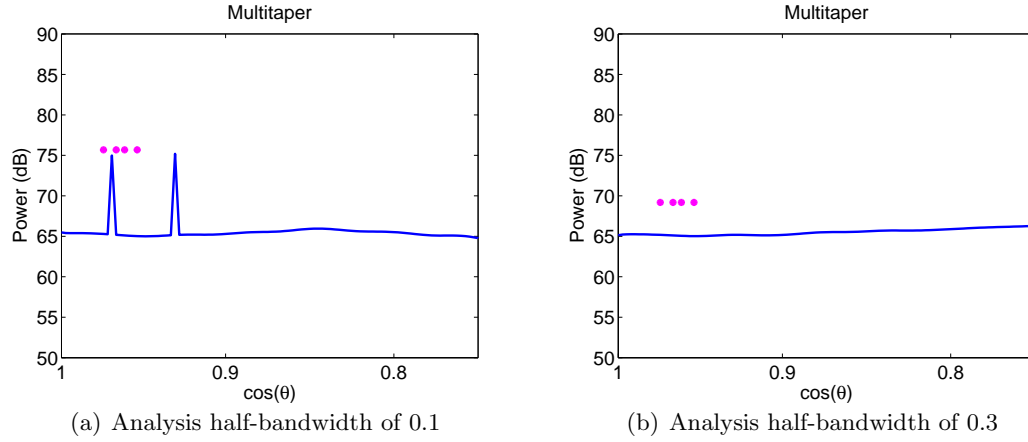


Figure 4.5: Analysis half-bandwidth for a frequency of 201Hz on HLA North. No plane wave is detected for an analysis band of  $\pm 0.3$

calculating such tapers. It is also noted that the current implementation of the multitaper processor is thought to be sub-optimal. Currently tapers are calculated around  $\theta = 0$  and the array response vectors do the downconversion. This is normal for uniformly spaced arrays but Bronez's method suggests tapers should be calculated at each look angle.

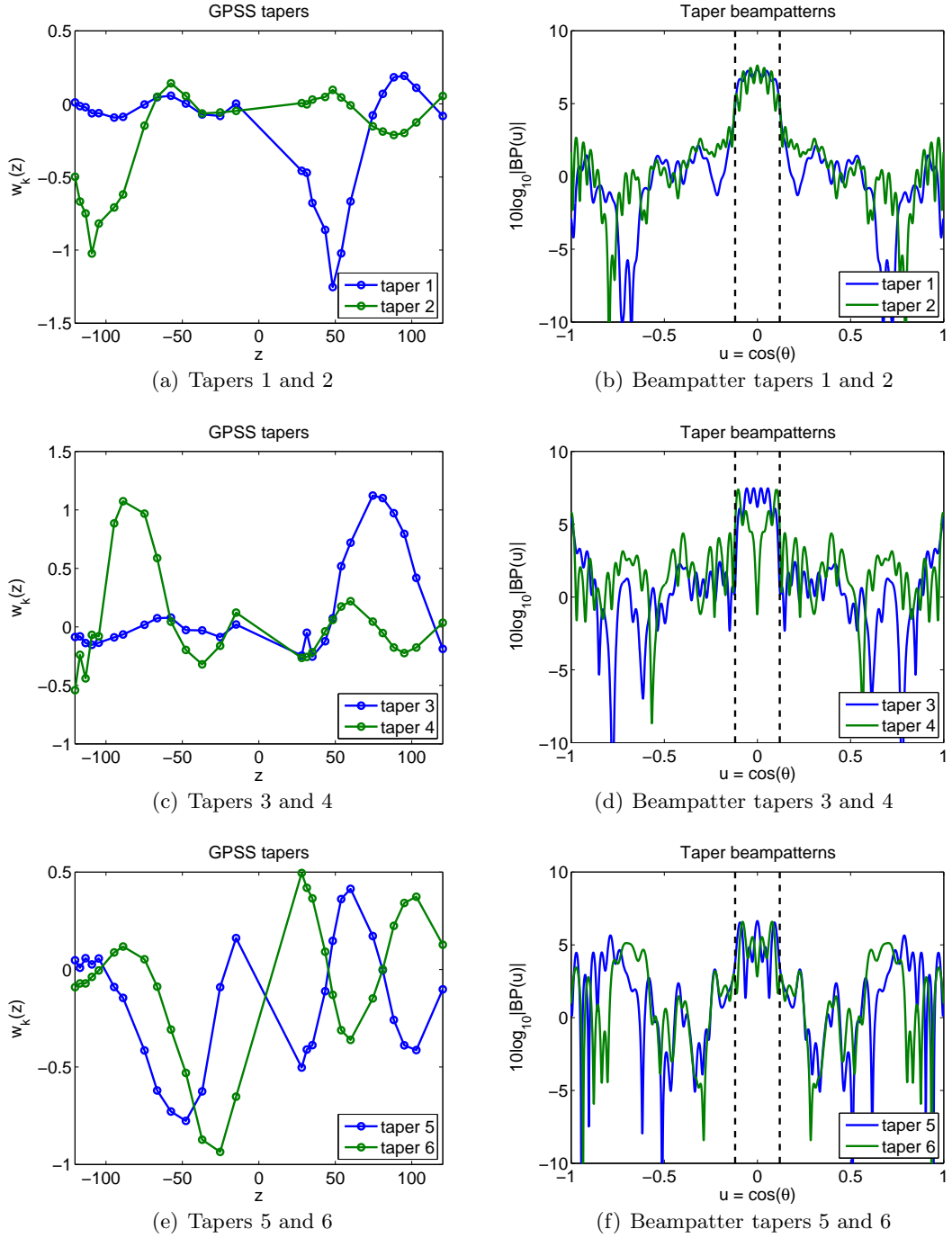


Figure 4.6: HLA North tapers and their beampatterns for an analysis bandwidth of  $0.1u$ . The dashed black lines show the analysis bandwidth.

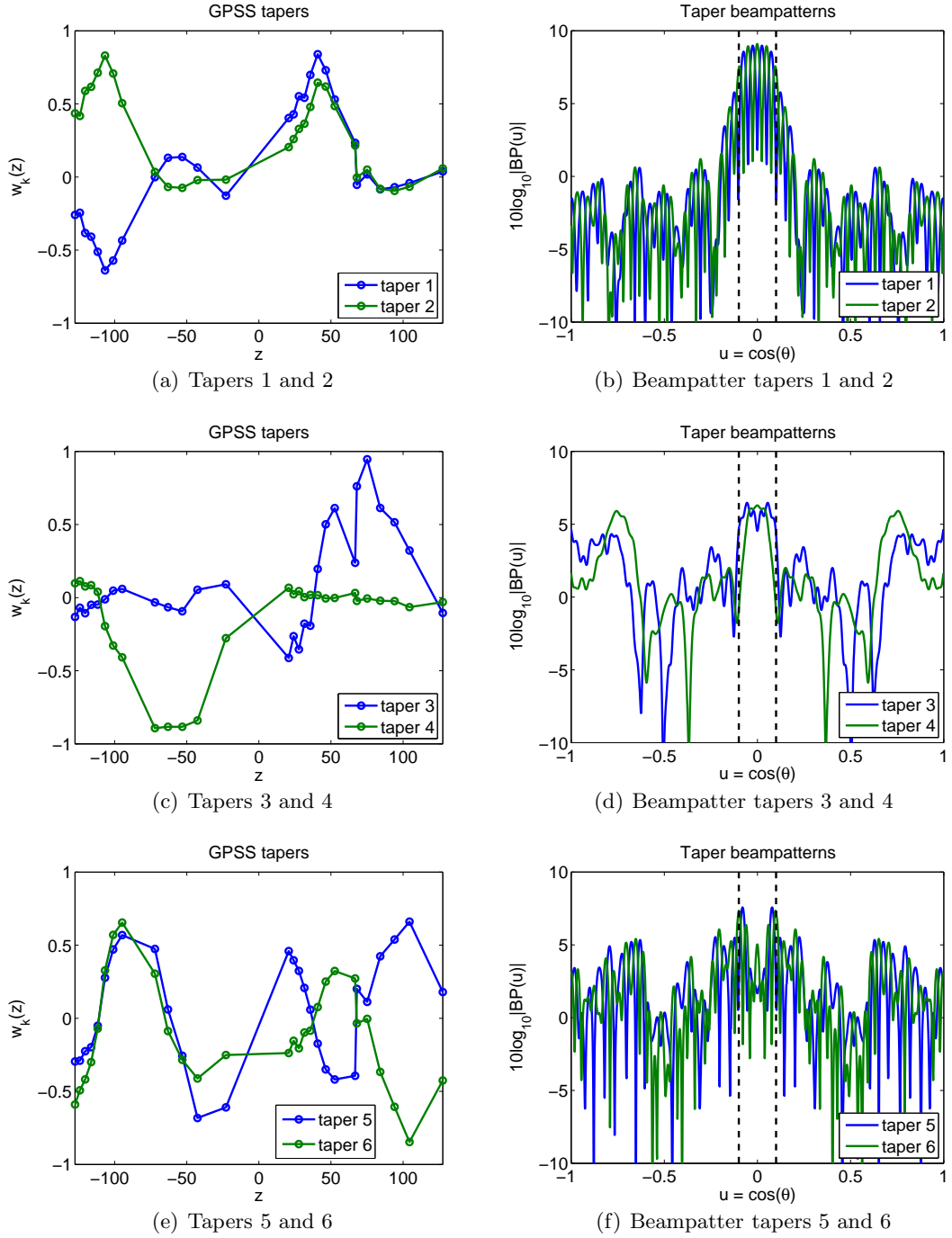


Figure 4.7: HLA South tapers and their beampatterns for an analysis bandwidth of  $0.1u$ . The dashed black lines show the analysis bandwidth.

## Chapter 5: Results

This chapter presents the results obtained from the conventional, MPDR and multitaper processors in the context of bearing estimation. The spatial spectrum is used to display the angular arrivals. Ray simulations are used predict the angles at which we expect to see arrivals from different paths originating at the source.

Ray theory and the simulation software is described. Then beamforming results from several cuts of data are shown at different ranges and azimuthal angles on HLA North followed by HLA South.

### 5.1 Ray Simulations

Ray theory provides an approximation of the possible propagation paths from source to receiver. It seeks solutions to the Helmholtz equation for the pressure field

$$\nabla^2 p + \frac{\omega^2}{c^2(\mathbf{x})} p = -\delta(\mathbf{x} - \mathbf{x}_s) \quad (5.1)$$

of the form

$$p(\mathbf{x}) = e^{jw\tau(\mathbf{x})} \sum_{i=0}^{\infty} \frac{A_i(\mathbf{x})}{(j\omega)^i} \quad (5.2)$$

The solutions rely on a high frequency assumption and vary depending on media characteristics [12] [13]. In the isovelocity case the solutions are straight lines connecting source and receiver directly or that may bounce off of the ocean surface or bottom.

For non-homogenous media such as the SWellEx-96 environment, where the sound speed is not constant, a numerical approximation must be computed with a ray code. An example of



ray paths that are used later are seen in Figure 5.7. In this case there are 3 paths computed via ray code; direct, surface bounce and a bottom-surface bounce paths. Figure 5.12 shows a longer range propagation where the paths bend a lot over range.

To verify that observed arrivals are indeed generated by the source the ray code "Eigen-Ray" has been used [13].

## 5.2 Number of Snapshots

The effect of snapshot numbers used for averaging and computing the covariance matrix  $\hat{\mathbf{R}}$  is briefly explored here. The source is at a close range of about 700 meters from HLA North as shown in Figure 5.1. Processed data for snapshot numbers of 1, 4, 10 and  $2N = 54$  is displayed in Figures 5.2, 5.3, 5.4 and 5.5. With 1 snapshot the CBF and multitaper show a main arrival clearly and CBF hints of 1 or two others. MPDR is relying almost exclusively on diagonal loading with only 1 snapshot so it closely resembles the CBF [1]. For the single snapshot case there is no gain to MPDR over CBF.

When averaging is introduced the multitaper processor detects more line components and shows multiple arrivals. The CBF is also less noisy. With larger amounts of averaging and a moving source, however, multitaper detects more and more line components from the different snapshots and the lobes of the CBF output become wider as they average in slightly offset lobes from more and more snapshots.

MPDR needs some amount of averaging just get a good estimate of  $\hat{\mathbf{R}}$ . At 4 snapshots it shows one lobe at the main arrival where the others are showing 2. As the number of snapshots increases, the lobe gets stronger but also wider ultimately suffering a similar fate to CBF at high numbers of snapshots and a moving source.

The processing herein uses 4 snapshots, a small amount of averaging, unless otherwise noted.

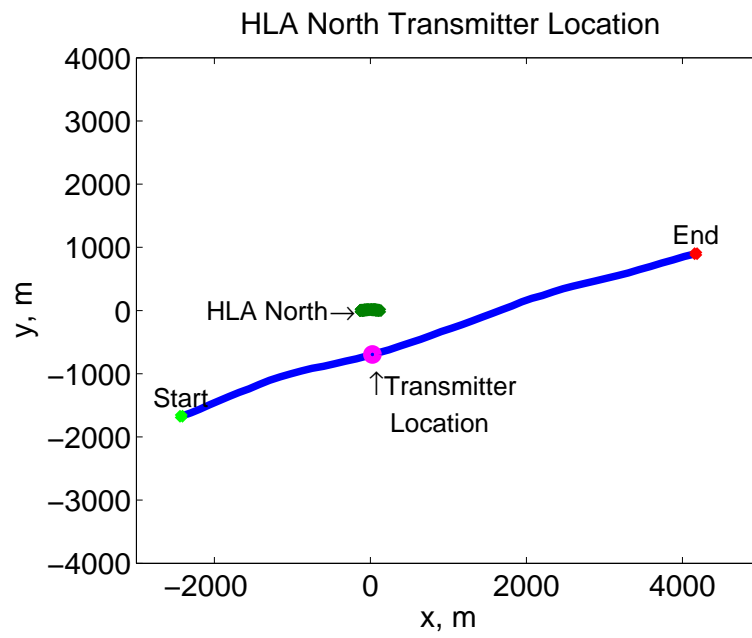
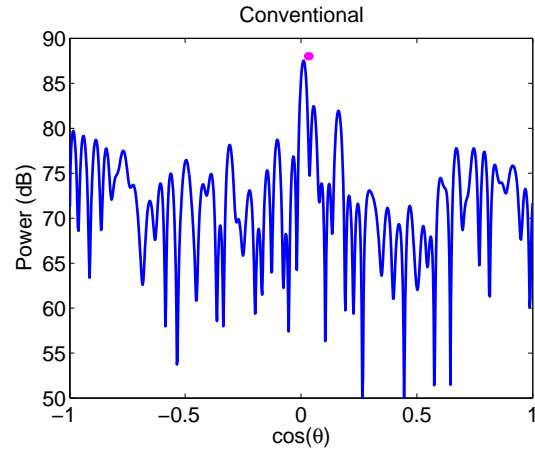
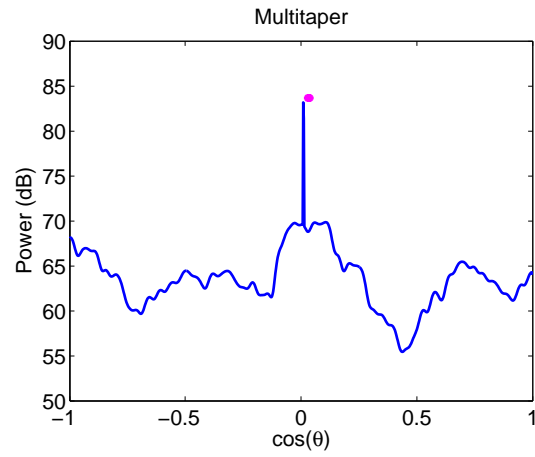


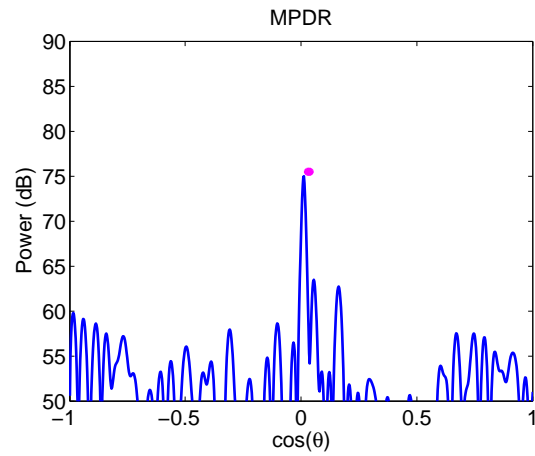
Figure 5.1: Position of transmitter at 18 minutes, 30 seconds



(a) Conventional

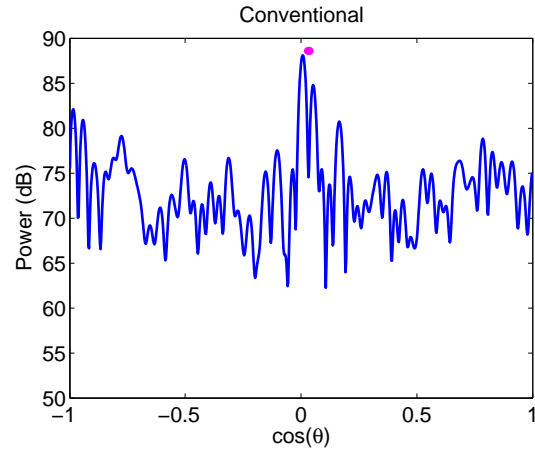


(b) Multitaper

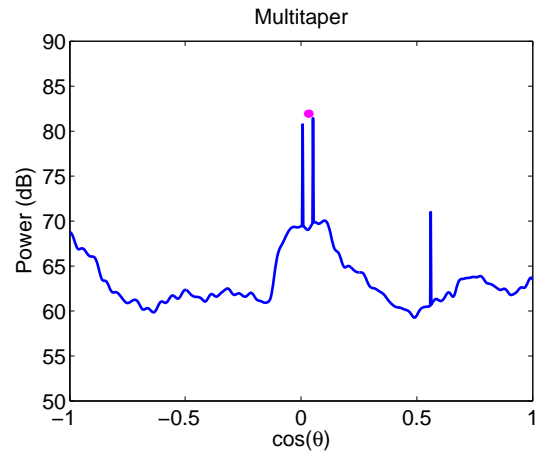


(c) MPDR

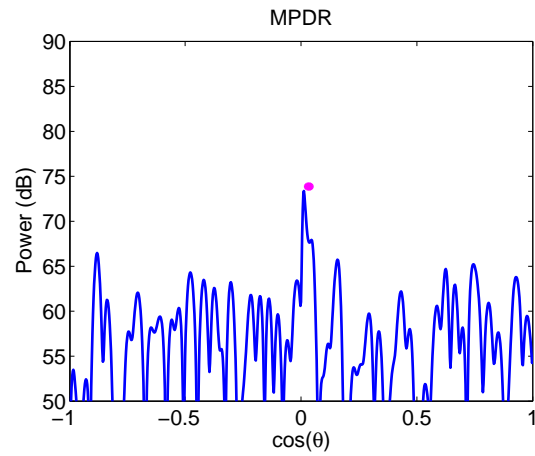
Figure 5.2: Spatial spectra at close range (about 750 m) to HLA North for 201Hz using 1 snapshot of data.



(a) Conventional

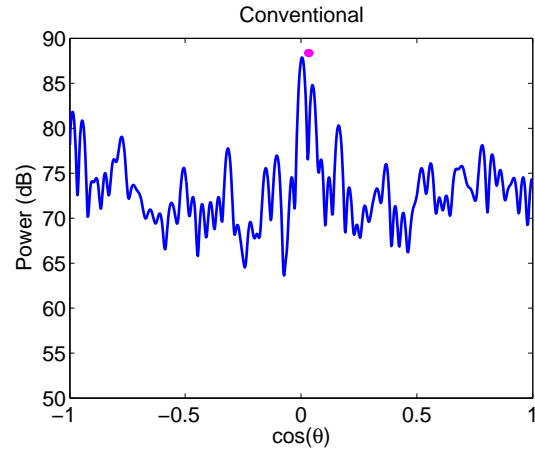


(b) Multitaper

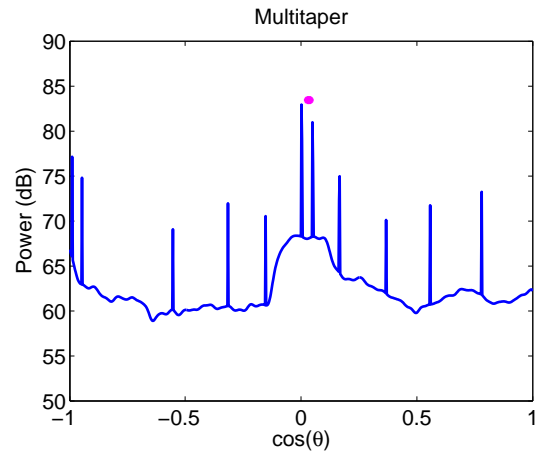


(c) MPDR

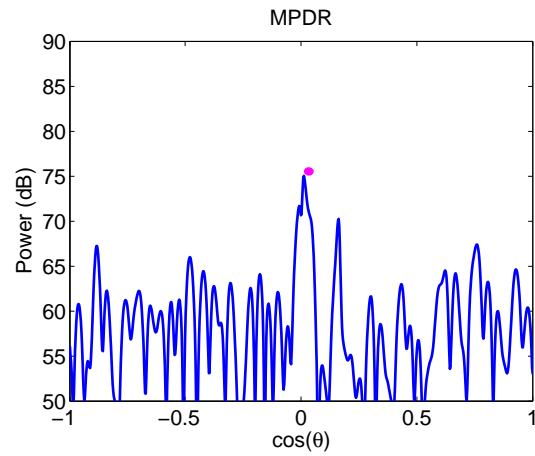
Figure 5.3: Spatial spectra at close range (about 750 m) to HLA North for 201Hz using 4 snapshot of data.



(a) Conventional

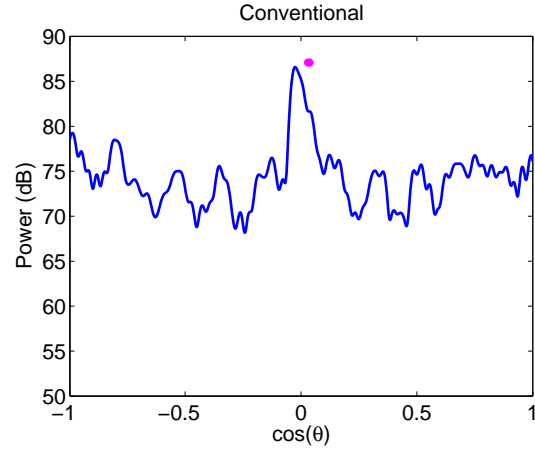


(b) Multitaper

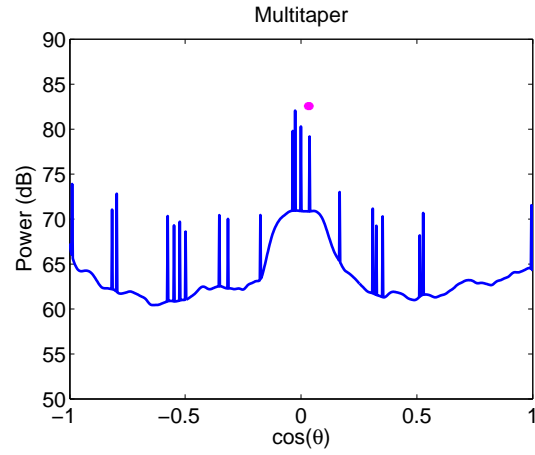


(c) MPDR

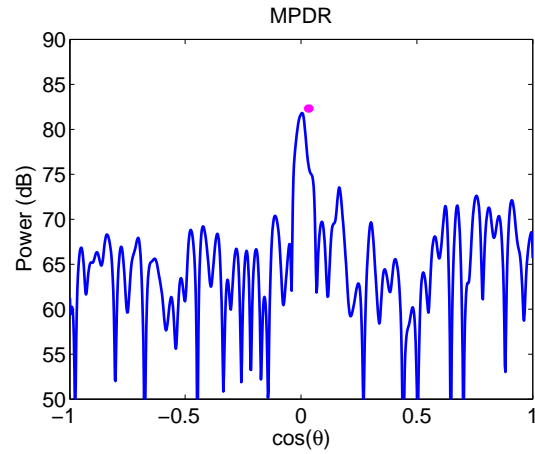
Figure 5.4: Spatial spectra at close range (about 750 m) to HLA North for 201Hz using 10 snapshots of data.



(a) Conventional



(b) Multitaper



(c) MPDR

Figure 5.5: Spatial spectra at close range (about 750 m) to HLA North for 201Hz using  $2N = 54$  snapshots of data.

## 5.3 Horizontal Line Array North

This section presents some results from HLA North. Close range data is explored for low and mid frequencies. Then long range data is processed for mid and high frequencies on the deep and shallow sources.

NOTE: the plots in this section have been normalized by their peak. They will be redone for the final report.

### 5.3.1 Close Range Source

This data is from 22 minutes, 13 seconds when the source is at a close range of about 750 meters and azimuthal angle of 316 degrees shown in Figure 5.6. The results of ray simulations displayed in Figure 5.7 suggest three arrivals might be observed. At this range, spherical wave beamforming is used.

Figures 5.8 and 5.9 show the spatial spectrum of the three beamformers for frequencies of 112 and 201 Hz respectively, representative of the low and mid frequencies transmitted. At low a frequency, Figure 5.8 shows there is too little resolution to view all the arrivals calculate by the ray simulations. for any beamformer to observe angular spread. All of the beamformers show energy at the direct path arrival of Figure 5.7 at this frequency.

At the mid-range frequency of 201Hz shown in Figure 5.9, the multitaper beamformer has three clear peaks. The conventional beamformer has two peaks easily seen but the third is harder to make out. The MPDR beamformer struggles to show a clear arrival at the source angle.

A bearing time record (BTR) for each beamformer is shown in Figure 5.10 for 201Hz. There are five contiguous time slices shown for each beamformer each using four snapshots, the current and three previous snapshots, in the computation of the spatial spectrum at each time. The time of 22.215 minutes corresponds to the line-plots shown in Figure 5.9

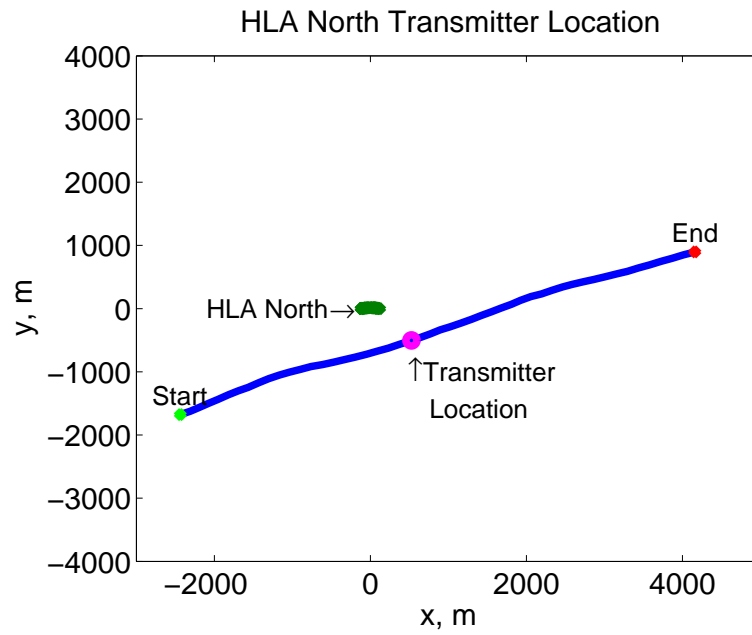


Figure 5.6: Position of transmitter at 22 minutes, 13 seconds

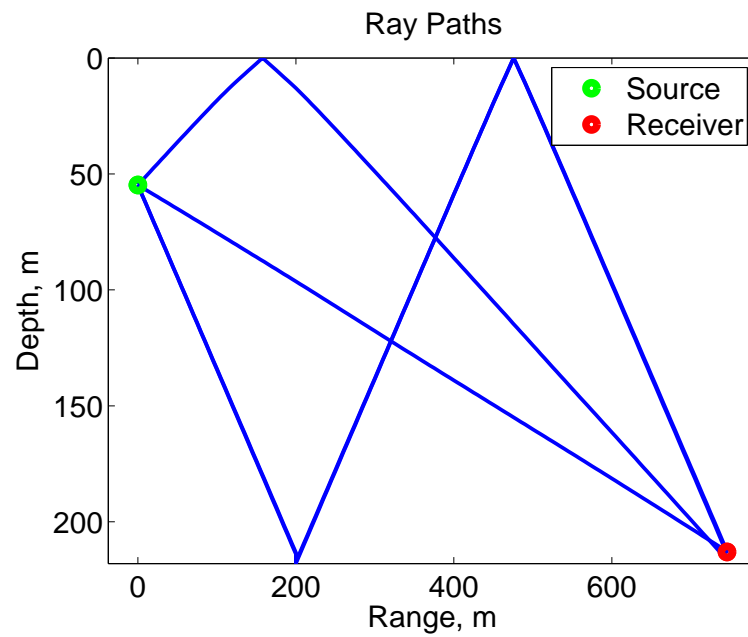


Figure 5.7: Ray paths from simulation at 750 meters



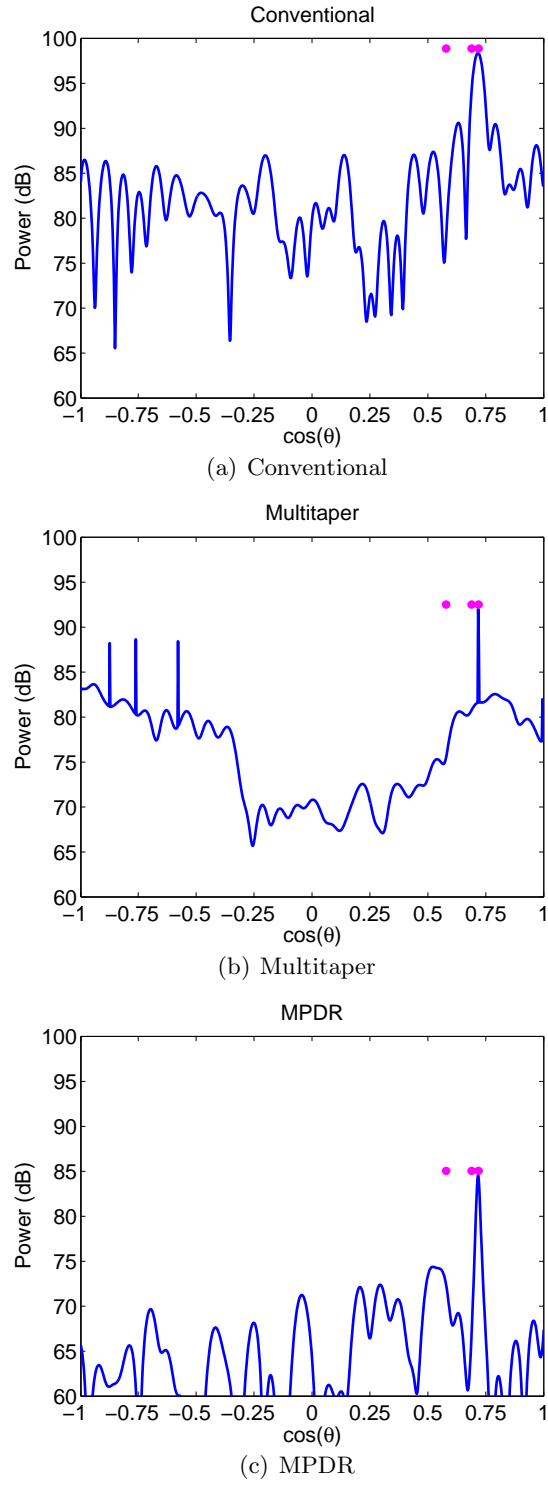
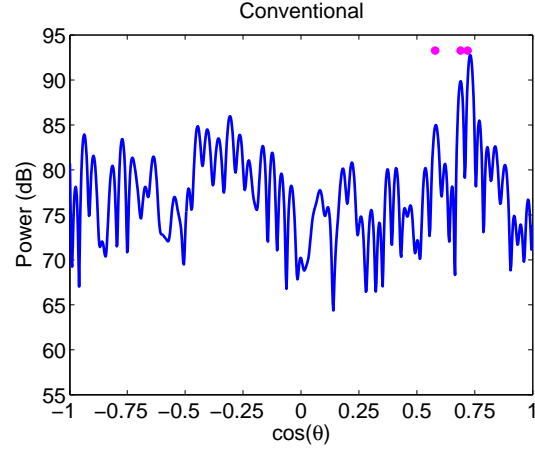
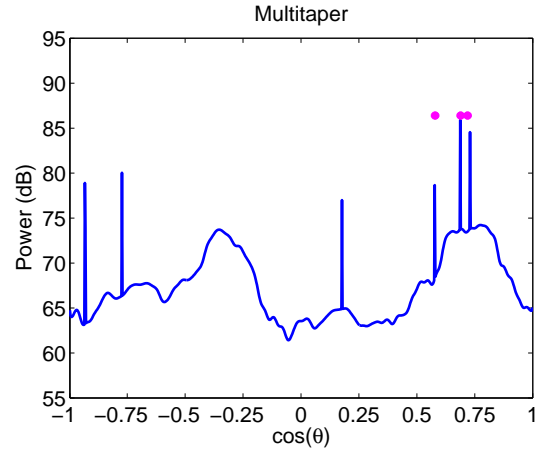


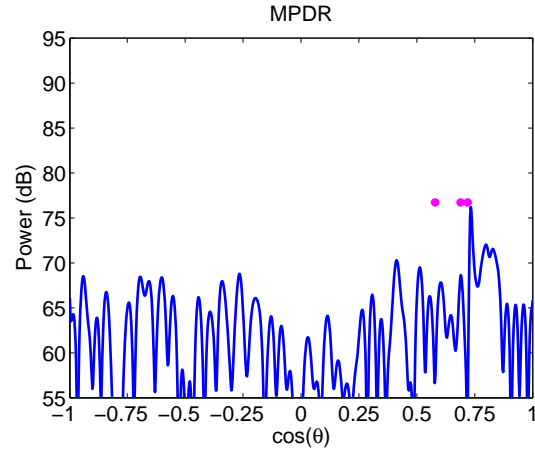
Figure 5.8: Spatial spectra at long range (about 4100 m) to HLA North for the 112Hz tone. 4 snapshots are used.



(a) Conventional

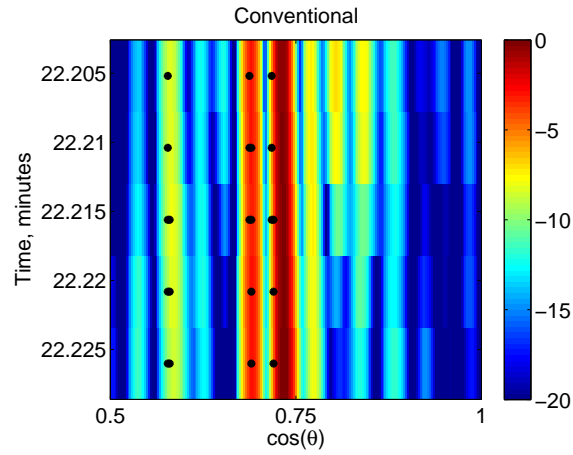


(b) Multitaper

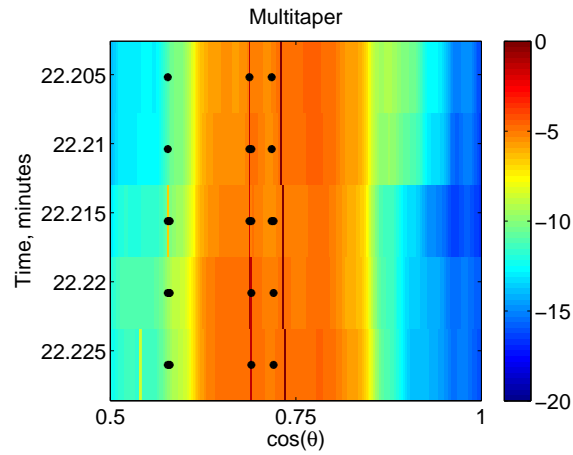


(c) MPDR

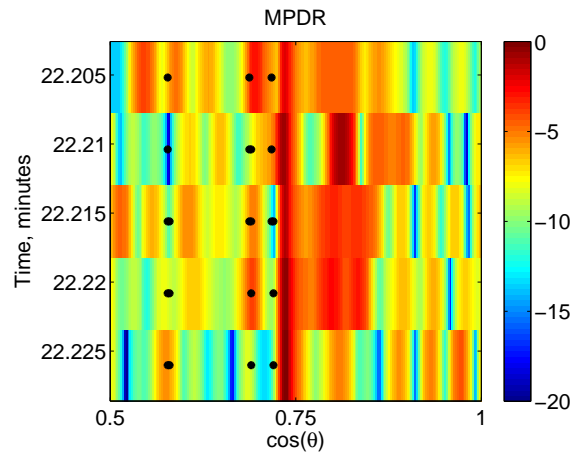
Figure 5.9: Spatial spectra at close range (about 750 m) to HLA North for 201Hz. 4 snapshots are used. The three arrivals estimated by ray simulations are easily seen in the output of the multitaper beamformer.



(a) Conventional



(b) Multitaper



(c) MPDR

Figure 5.10: Raster plots of spatial spectra at close range (about 750 m) to HLA North for 201Hz on a dB scale. 4 snapshots are used at each time. The black marks indicate the arrivals from ray simulations

### 5.3.2 Long Range Source

A cut of data at a long range of about 4100 meters as shown in Figure 5.11. The ray simulations shown in Figure 5.12 show a number of potential multipath arrivals for this data. However, at a long range less spread is expected between the paths.

#### Deep Source Tones

Figures 5.13 and 5.14 show the spatial spectrum of the plane wave beamformers for a frequencies of 201 and 388 Hz over  $1 \geq \cos(\theta) \geq -1$  ( $0 \leq \theta \leq 180$ ). The clearest example of angular spread is for the multitaper case at 201 Hz where there are two distinct arrivals. Multipath arrivals are not apparent at 388Hz for any processor. From the information shown in Figure 4.3, the tapers are expected to perform poorly at around 400Hz on this array with lots of energy in the sidelobes.

If the number of snapshots is increased to  $2N = 54$ , as shown in Figure 5.15, multiple arrivals become clearer in the CBF output. The MPDR output is improved but still lacks a clear arrival at the source angle.

Returning to the case of 4 snapshots, Figure 5.16 shows a close up of the arrivals around the source angle. Note that Figure 5.16 is plotted versus  $\theta$  directly. The ray simulation arrivals do not match up exactly but the closes ones are within fractions of a degree of the arrival on the left. However, the spread of the ray approximation is about 4.3 degrees where as the spread of of the two beamformed arrivals are about 7 degrees. That raises some concern that the second arrival is not from multipath but from some other source or that the ray simulation is not accurate enough to solve all the paths that are observed in this case. Regardless, the multitaper has pulled out the second peak much more clearly than the conventional beamformer.

#### Shallow Source Tones

Figure 5.17 shows the ray path estimates for the shallow source at 4100 meters range. Figure 5.18 shows the results of processing a mid-range frequency, 198Hz. There is a clear

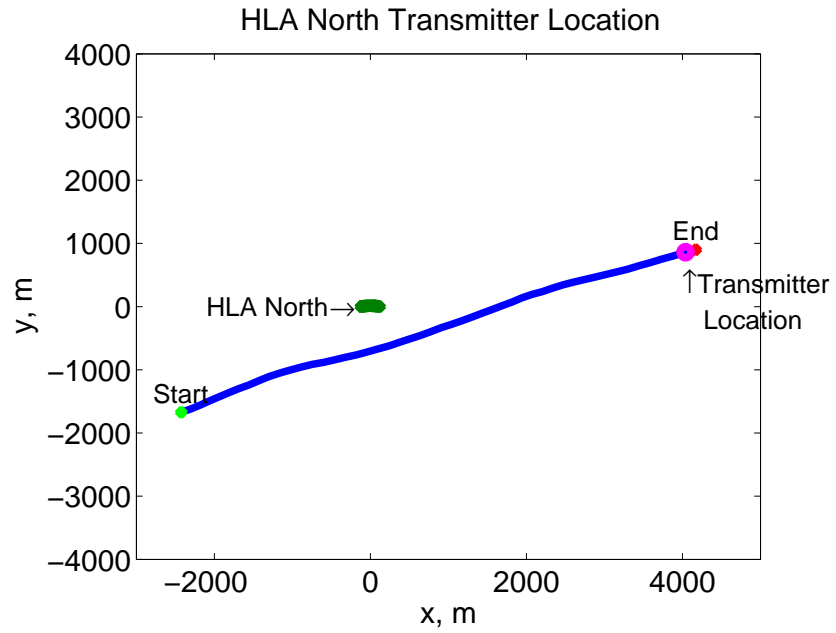


Figure 5.11: Position of transmitter at 48 minutes, 7 seconds

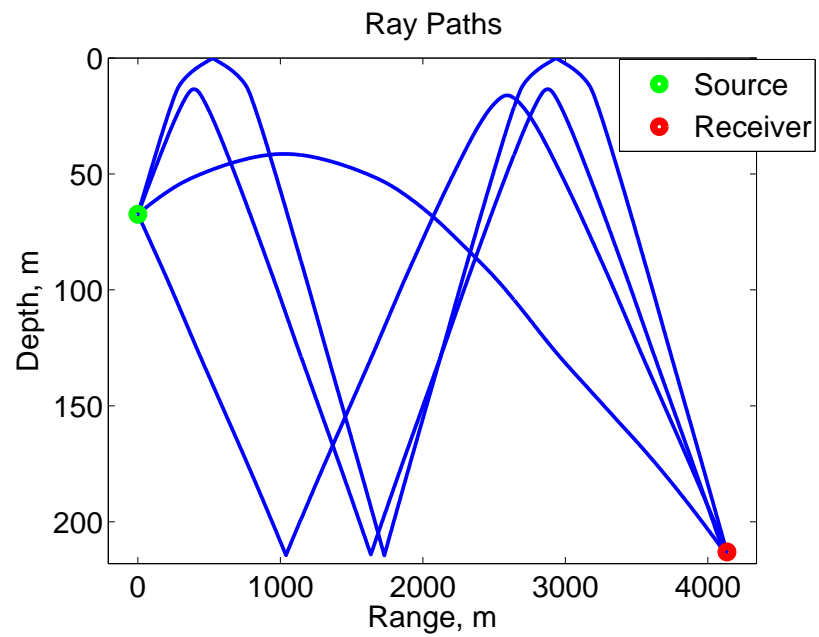
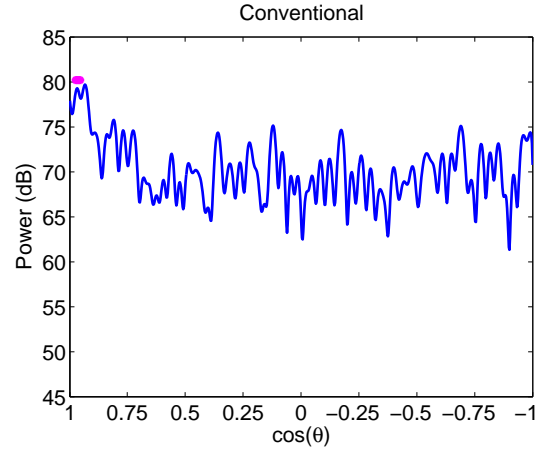
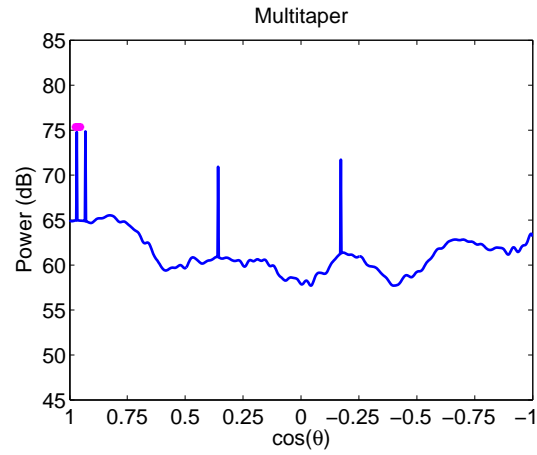


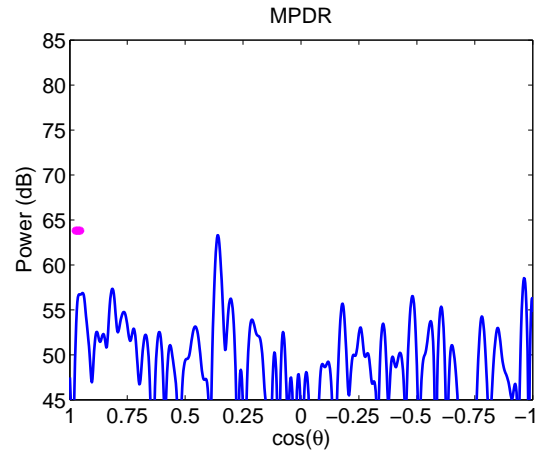
Figure 5.12: Ray paths from simulation at 4100 meters



(a) Conventional

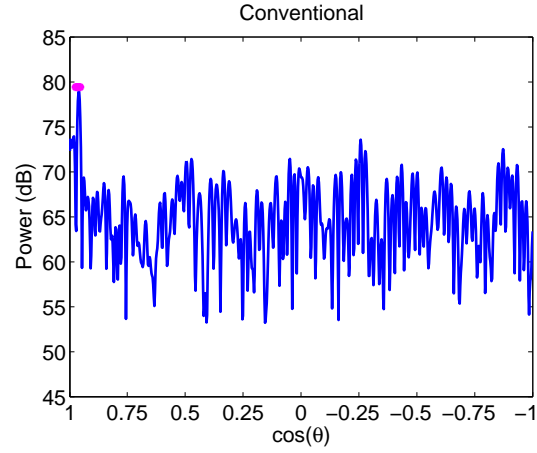


(b) Multitaper

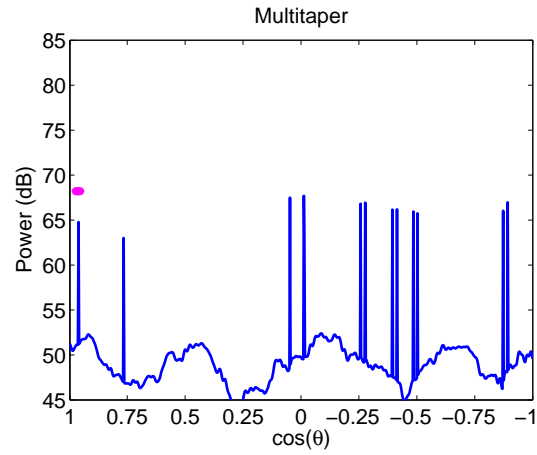


(c) MPDR

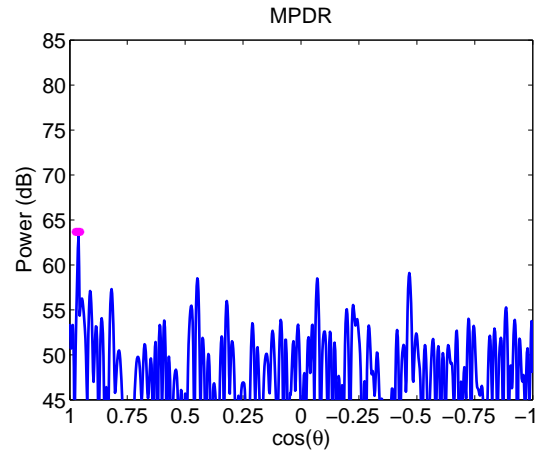
Figure 5.13: Spatial spectra at long range (about 4100 m) to HLA North for the high level tone 201Hz. 4 snapshots are used. The three arrivals estimated by ray simulations are easily seen in the output of the multitaper beamformer.



(a) Conventional

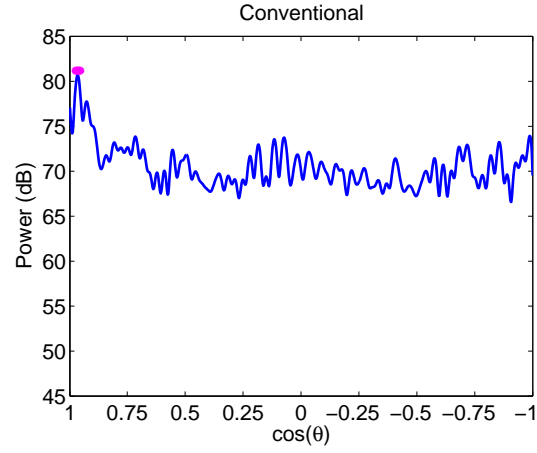


(b) Multitaper

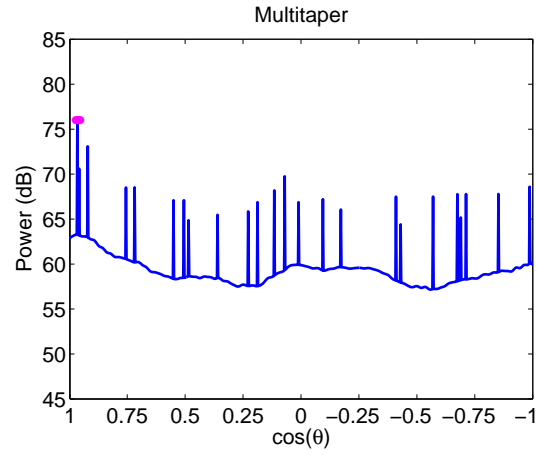


(c) MPDR

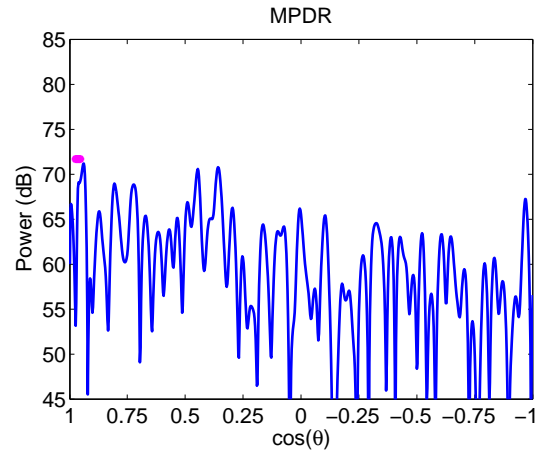
Figure 5.14: Spatial spectra at long range (about 4100 m) to HLA North for the high level tone 388Hz. 4 snapshots are used. No multipath is apparant on any beamformer at this frequency.



(a) Conventional



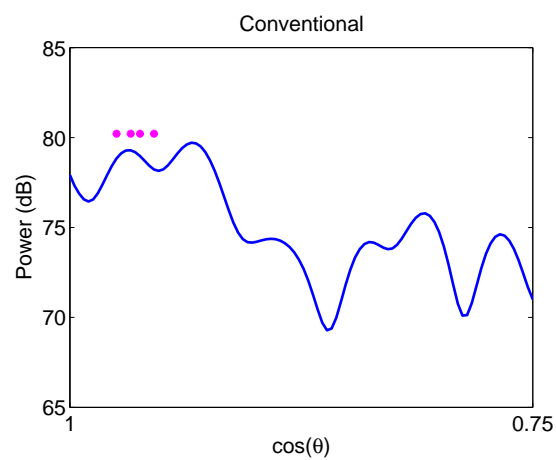
(b) Multitaper



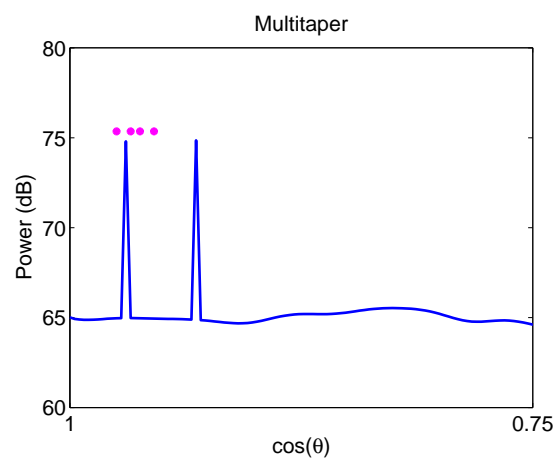
(c) MPDR

Figure 5.15: Spatial spectra at long range (about 4100 m) to HLA North for the high level tone 201Hz.  $2N = 54$  snapshots are used.





(a) Conventional



(b) Multitaper

Figure 5.16: Zoomed in on spatial spectra at long range (about 4100 m) to HLA North for the high level tone 201Hz. 4 snapshots are used.

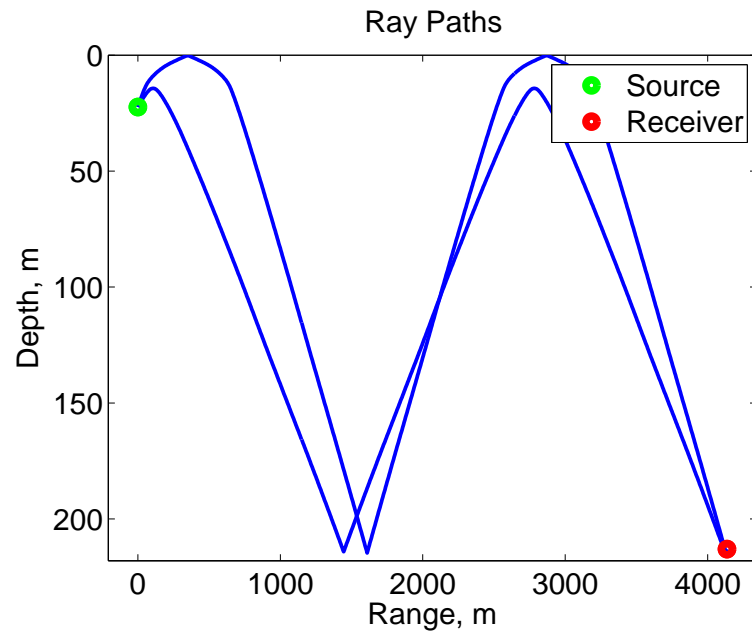
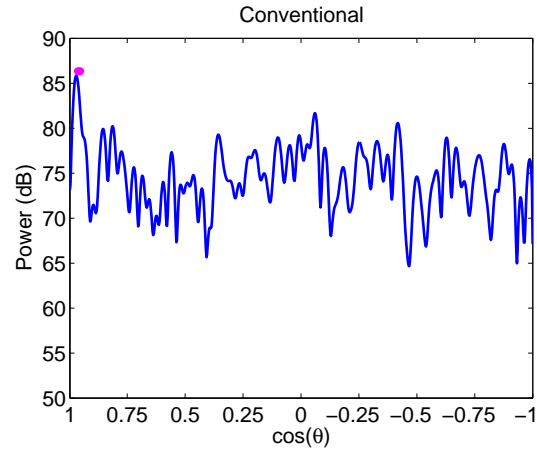
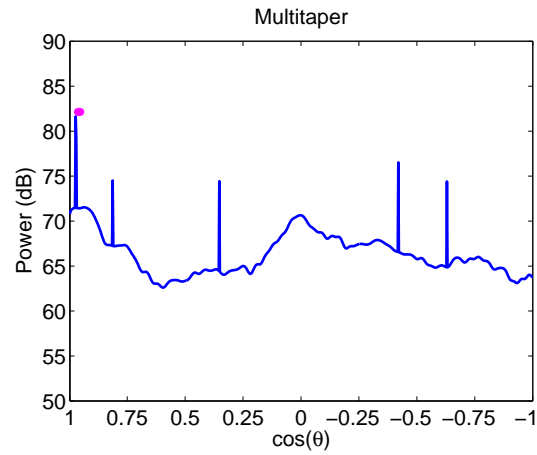


Figure 5.17: Shallow source ray paths from simulation at 4100 meters

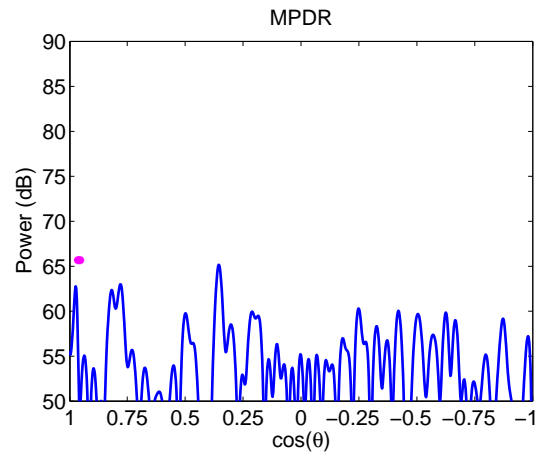
arrival in the CBF and multitaper processor from the shallow source at that range. MPDR also displays some energy there.



(a) Conventional



(b) Multitaper



(c) MPDR

Figure 5.18: Spatial spectra at long range (about 4100 m) to HLA North for the shallow source tone 198Hz. 4 snapshots are used.

## 5.4 Horizontal Line Array South

The section explores data from the south array at a mid range of about 2600 meters. High and level tones are processed followed by low level tones from the same snapshots.

### 5.4.1 High Level Tones

Data from the source at 2600 meters as shown in Figure 5.19 is processed. From the results of the raycode in Figure 5.20 there are potentially three arrivals to observe.

Processing results for frequency 201Hz are shown in Figure 5.21. The beamformers all appear to have something going on around the calculated arrival angles. CBF has produced one wide mainlobe, perhaps due to averaging multiple snapshots, and MPDR has a very low level peaks but nothing that really inspires confidence that there is in fact an arrival there. The multitaper processor, however, has produced three peaks. A closer look in Figure 5.22 shows the ray simulations and processor output are very similar. They are similar in structure and off from one another by less than a degree. It looks promising for the multitaper processing here.

A BTR for the three processors are shown in Figure 5.23. Each snapshot within the BTR is normalized to its peak energy. The snapshots from Figure 5.21 are shown at time 20.1 minutes. The multitaper processor consistently shows 3 arrivals over time while the others do not.

### Low Level Tones

Figures 5.24 and 5.25 show the results of processing mid-frequency range, lower power level tones of 204 and 207 Hz respectively. The tones are from the 2nd and 3rd tonal set transmitting at 26dB and 30dB down from the high level tones. There appears to be some energy at the calculated arrival angle for the 204 Hz conventional beamformer and the the multitaper processor detects a line component. At 207 Hz, there does not appear to be arrivals where they are expected in any of the processors.

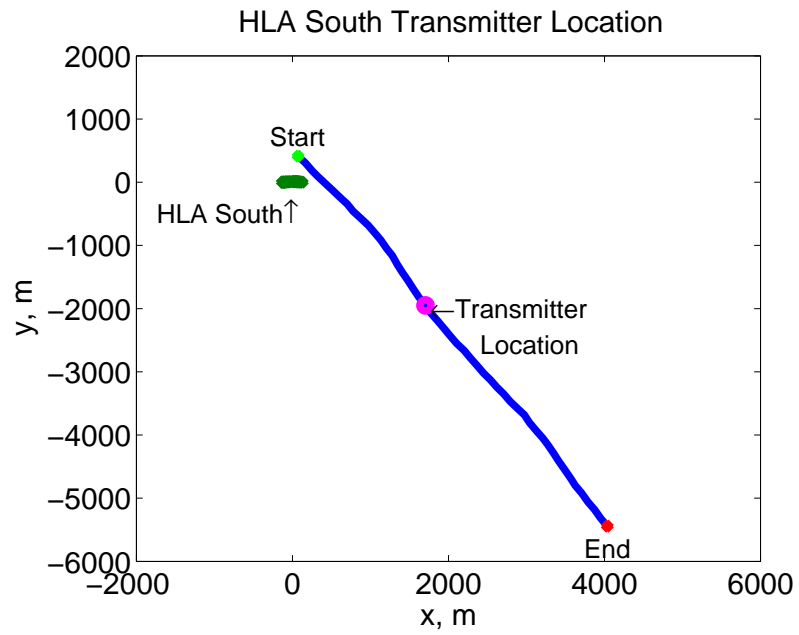


Figure 5.19: Position of transmitter at 20 minutes, 6 seconds

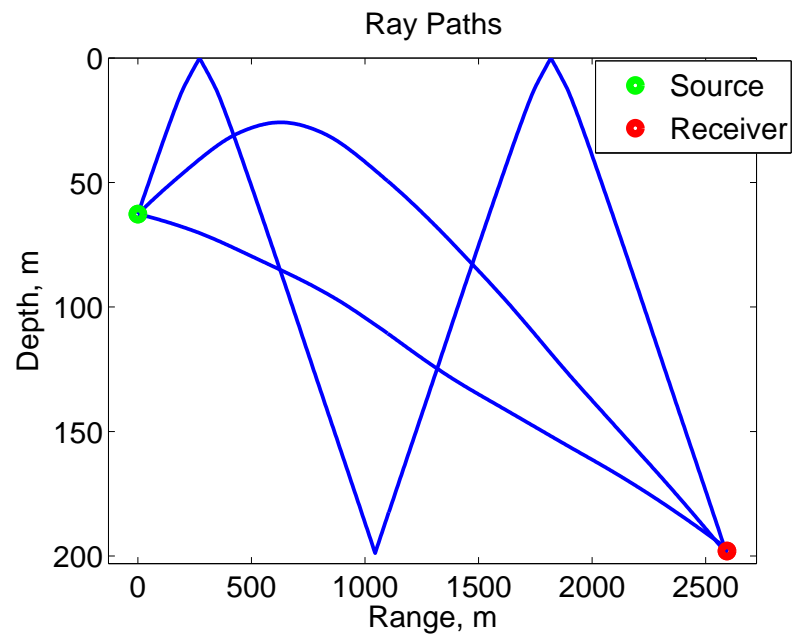
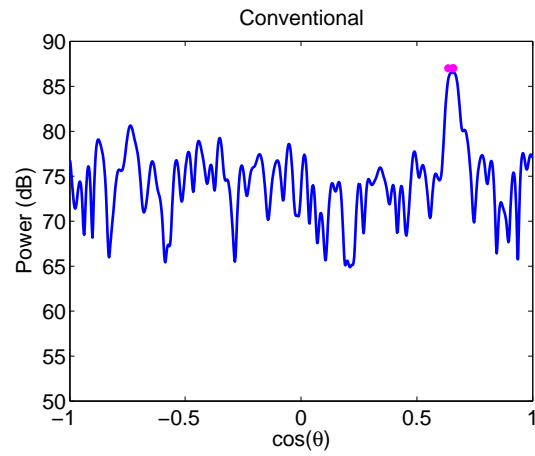
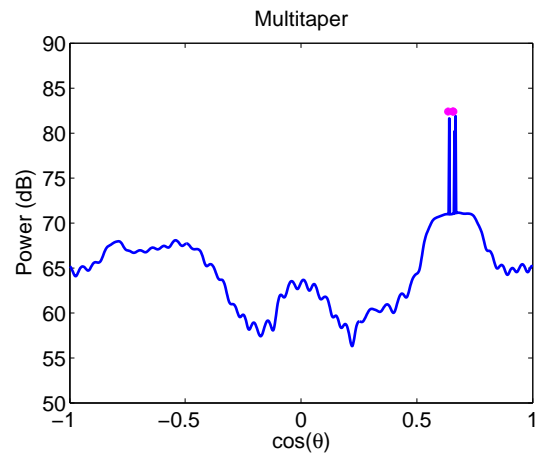


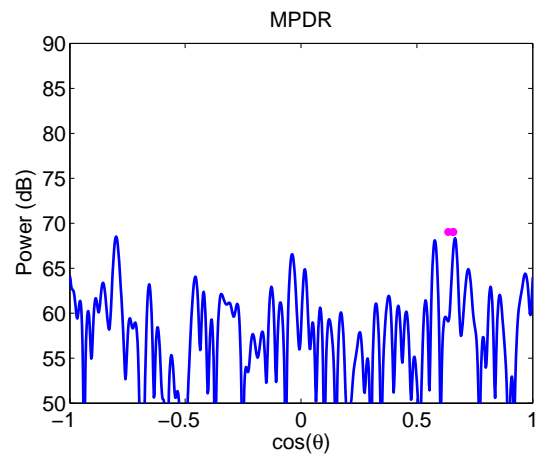
Figure 5.20: Ray paths from simulation at 2600 meters



(a) Conventional



(b) Multitaper



(c) MPDR

Figure 5.21: Spatial spectra at mid range (about 2600m) to HLA South for 201Hz. 4 snapshots are used.

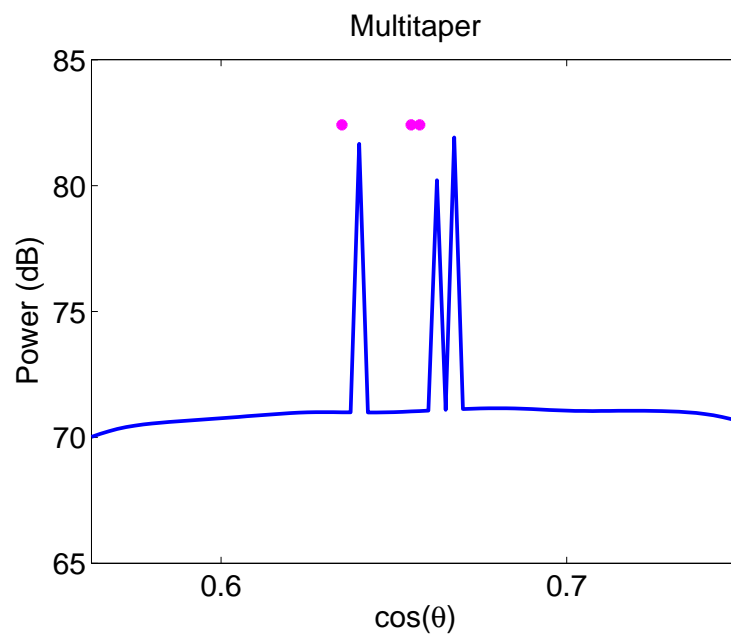
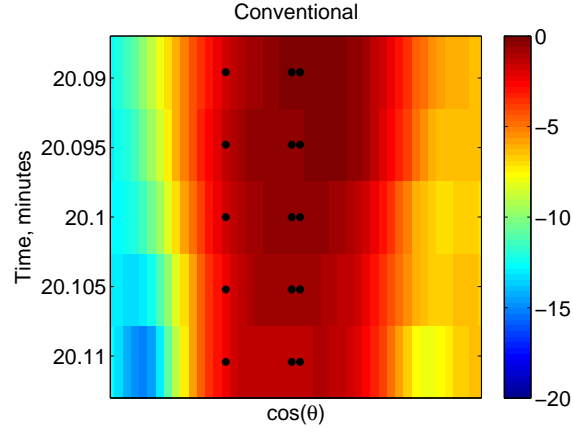
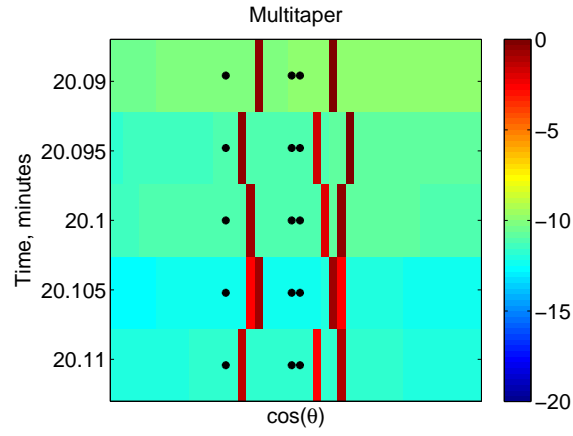


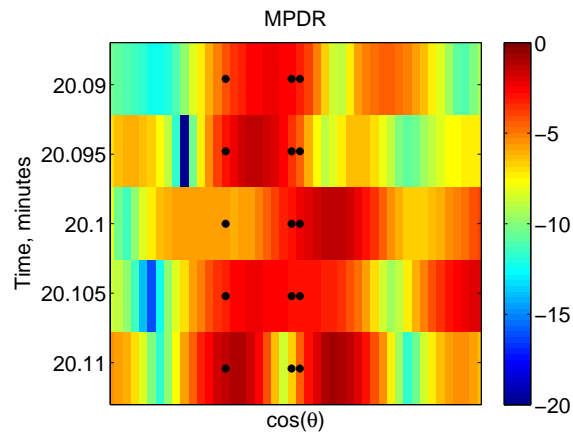
Figure 5.22: Position of transmitter at 20 minutes, 6 seconds



(a) Conventional



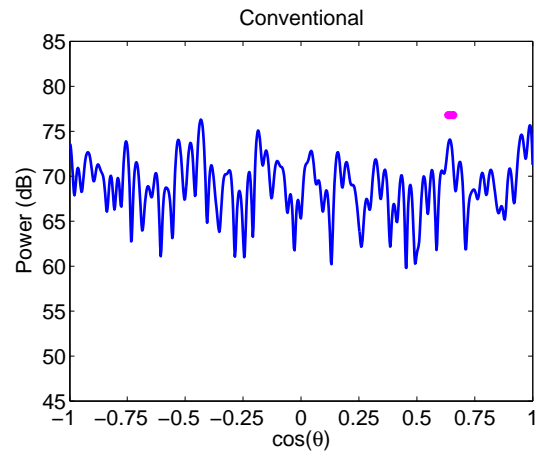
(b) Multitaper



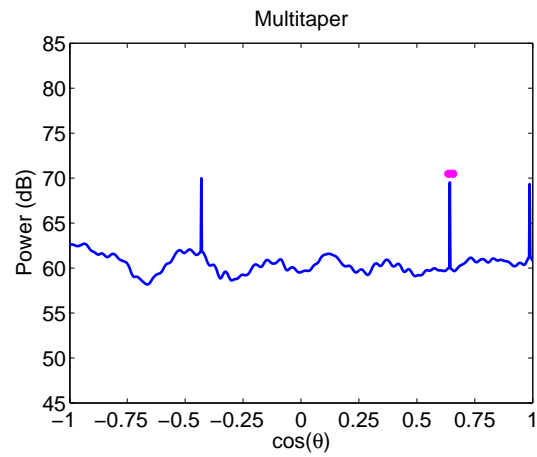
(c) MPDR

Figure 5.23: BTR at mid range (about 2600 m) to HLA South for 201Hz on a dB scale. 4 snapshots are used at each time. The black marks indicate the arrivals from ray simulations

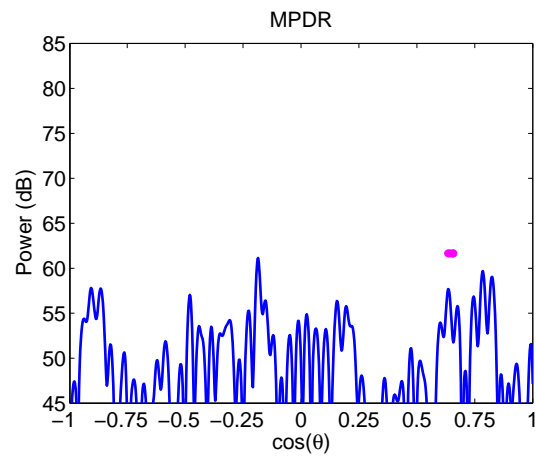




(a) Conventional

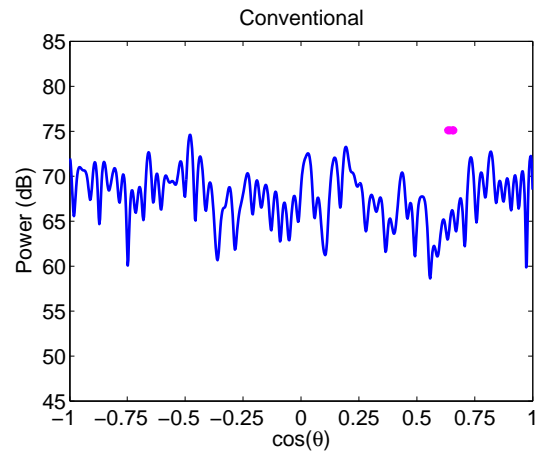


(b) Multitaper

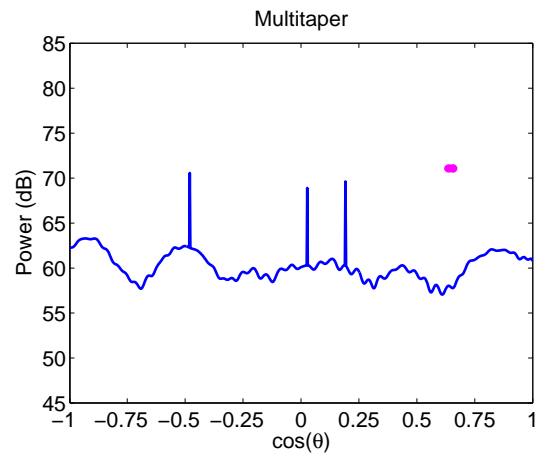


(c) MPDR

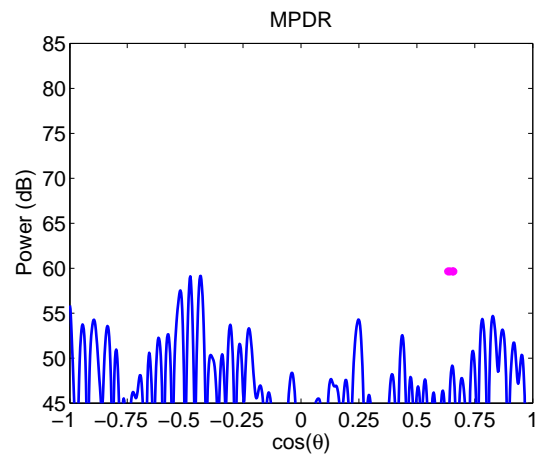
Figure 5.24: Spatial spectra at long range (about 2600 m) to HLA South for the low level tone 204Hz. 4 snapshots are used.



(a) Conventional



(b) Multitaper



(c) MPDR

Figure 5.25: Spatial spectra at long range (about 2600 m) to HLA South for the low level tone 207Hz. 4 snapshots are used.

## 5.5 Summary

This chapter presented the results of processing data from the SWellEx-96 HLA North and South using the methods of CBF, MPDR and the multitaper array processor. Ray simulations were used to verify the results. The snapshot issue was briefly explored with large snapshot numbers found to be of concern in this dataset with a moving source. With a reduced snapshot number, the multitaper processor showed promising signs of angular spread in the arrivals. However, it currently suffers some mismatch in scaling at close range that prevents it from detecting the line component correctly, apparant in the humps around many of the arrivals.

## Chapter 6: Conclusion

This chapter discusses the results of angular spread observation. A summary of the methods and their potential pitfalls is given. Then the results of processing the SWellEx-96 data are discussed. A brief discussion of potential sources of mismatch is presented. Finally, future work to improve performance of the multitaper processor in the SWellEx-96 case is discussed.

### 6.1 Concluding Comments

The SWellEx-96 experiment provides a freely available dataset with which to test and compare methods of generating spatial spectrum for the purpose of bearing estimation. The conventional and MPDR beamformers are standard, well-studied array processing methods. The advantage of the CBF is that it is simple; the beamformer is just the spatial matched filter of a wavefront impinging on the array from an angle of interest. However, weaker multipath arrivals potentially get lost in the high sidelobes of this method.

The MPDR beamformer has a potential advantage for observing multipath arrivals in that it attempts to null out arrivals from directions other than the look direction so a weak multipath arrival might not be lost in the sidelobes of a stronger arrival. However, it requires an estimate of the covariance matrix  $\mathbf{R}$  which requires many snapshots of data. Diagonal loading can be used to stabilize the inverse,  $\mathbf{R}^{-1}$ , in the low snapshot case but it reduces the nulling effect.

The multitaper processing framework presented in Chapter 4 has the potential to reduce the sidelobe problem of the CBF and operate on a small number of snapshots.

The results in Chapter 5 show promise of observing angular spread in the SWellEx-96 data with multitaper array processing. Comparing the three methods, the CBF does well

in displaying a main arrival but often has problems showing multiple arrivals. The sidelobe performance is a concern as the multipath seems to be buried in them in some cases. In the MPDR results, it is often hard to see a clear peak at the calculated angles of arrival. This could be due to the reduced number of snapshots used in the covariance matrix estimation. The multitaper processor had the clearest examples of angular spread in the cases examined here.

## 6.2 Mismatch Issues

Mismatch from any number of sources is a concern with all methods. When forming the array response vectors, there is an inherent mismatch in the wavenumber  $\mathbf{k}$ , as a constant soundspeed is assumed when computing the wavelength  $\lambda$ . However, the SWellEx-96 waveguide has a depth-dependent sound speed.

The environmental data used by the ray code is not range dependent. The sound speed profile was taken at one point near the experiment about 5 hours beforehand. Also, the depth of the water column was assumed to be constant and is set to the depth of the array in the simulations. However, the bottom actually varied in depth from about 180 to 220 meters throughout the tow.

At this point there appears to be a mismatch in the scaling of the array response vector at close range. The humps in the multitaper estimated spectra around many line components appears to be residual power from improperly estimated line components.

There is also mismatch in the spherical wave beamforming. The range used to generate the array response vector assumes straight line propagation. This assumption is not always true for the direct path and certainly not for the multipath arrivals.

## 6.3 Future Work

More work needs to be done on the taper design for the SWellEx-96 arrays. As noted in Chapter 4 the tapers used for processing have a small analysis band with high leakage.

This is counter to Bronez's recommendation to widen the analysis band to reduce leakage. However, better results were observed with the narrower analysis band. Also as noted in Chapter 4, the tapers may need to be recalculated for look angles other than  $\theta = 0$ .

As previously noted, the weight vector for close range data needs to be improved, likely with range dependent scaling at each element.

## Bibliography

## Bibliography

- [1] H. L. Van Trees, *Optimum Array Processing*. New York, NY: John Wiley and Sons, Inc., 2002.
- [2] D. H. Johnson and D. E. Dudgeon, *Array Signal Processing. Concepts and Techniques*. P T R Prentice-Hall, Inc., 1993.
- [3] D. G. Manolakis, V. K. Ingle, and S. M. Kogon, *Statistical and Adaptive Signal Processing*. Artech House, 2005.
- [4] D. J. Thomson, "Spectrum estimation and harmonic analysis," *Proceedings of the IEEE*, vol. 70, pp. 1055–1096, September 1982.
- [5] K. E. Wage, "Multitaper array processing," *Proceedings of the 41st Asilomar Conference on Signals, Systems, and Computers*, pp. 1242–1246, November 2007.
- [6] T. P. Bronez, "Nonparametric spectral estimation of irregularly sampled multidimensional random processes," Ph.D. dissertation, Arizona State University, Phoenix, 1985.
- [7] J. Murray, "Welcome to the SWellEx-96 experiment," San Diego, 2003. [Online]. Available: <http://www.mpl.ucsd.edu/swellex96/index.htm>
- [8] R. A. Serway and R. J. Beichner, *Physics for Scientists and Engineers*, 5th ed. Saunders College Publishing, 2000, vol. 1.
- [9] P. Welch, "The use of the Fast Fourier Transform for the estimation of power spectra," *IEEE Transactions on Audio and Electroacoustics*, pp. 70–73, June 1967.
- [10] Y. Jin and B. Friedlander, "A cfar adaptive subspace detector for second-order gaussian signals," *IEEE Transactions on Signal Processing*, pp. 871–884, March 2005.
- [11] T. P. Bronez, "Spectral estimation of irregularly sampled multidimensional processes by generalized prolate spheroidal sequences," *IEEE Transactions on Acoustics, Speech, and Signal Processing*, vol. 36, no. 12, pp. 1862–1873, December 1988.
- [12] F. Jensen, W. Kuperman, M. Porter, and H. Schmidt, *Computational Ocean Acoustics*. New York: AIP Press, 1994.
- [13] B. D. Dushaw and J. A. Colosi, "Ray tracing for ocean acoustic tomography," *Applied Physics Laboratory*, 1998.



## Curriculum Vitae

Richard Wheelock was born in the USA in 1979 where he lived until age 10 when he and his family moved to Australia for 8 years. With the Australian school year running January through December and arriving in June, he missed half of grade 4 and has never quite recovered. In 1998 he returned to the USA and began work on his Bachelors degree in Electrical and Computer Engineering at George Mason University (GMU).

Graduating in 2002 with his B.S., Richard already had a couple years industry experience having helped his father start a signal processing systems company, n~ask, inc., in 2000. The company has grown from a basement operation to over 20 employees around the country.

He took a break from the small business returning to GMU as a Graduate Research Assistant to Dr. Kathleen Wage in Fall 2006.

Richard plans to return to family business upon completion of his Masters work.